UNIVERSIDAD DE CONCEPCIÓN
FACULTAD DE CIENCIAS FÍSICAS Y MATEMÁTICAS
PROGRAMA DE DOCTORADO EN CIENCIAS FÍSICAS

CINEMÁTICA Y DINÁMICA DE GAS IONIZADO EN EL NÚCLEO DE LA GALAXIA M87

Por: Juan David Osorno Quiceno

Tesis presentada a la Facultad de Ciencias Físicas y Matemáticas de la Universidad de Concepción para optar al grado académico de Doctor en Ciencias Físicas.

Septiembre de 2023

Concepción, Chile

Profesor Guía: Neil Mark Nagar

A mi familia, por todo su apoyo y paciencia.

AGRADECIMIENTOS

Aprovecho este espacio para agradecer a todas las personas que, de manera direta o indirecta, contribuyeron a que lograra culminar este trabajo. A mi supervisor Neil Nagar, por darme la oportunidad de ingresar a esta maravillosa rama de la ciencia y servir de guía durante mis estudios. A los miembros del comité evaluador, por su disposición a separar un poco de su tiempo para ayudarme a sacar adelante este trabajo. A mis amigos de la universidad (de Astronomía y del Doctorado en Ciencias Físicas) y los que he conocido en Concepción (chilenos y de intercambio), especialmente los del grupo de juegos de mesa; ha sido todo un placer compartir con ellos durante estos años.

Finalmente, quiero agradecer a mi familia, mi mamá Soledad, mi papá Mario y mi hermana Manuela, por todo su apoyo incondicional; este logro también es su logro.

Resumen

La medición de la masa del agujero negro en la galaxia M87, basada en su cinemática estelar, es el doble de la determinada mediante la cinemática del gas ionizado, con una discrepancia entre ambos mayor a 3σ. Para comprender mejor las razones del desacuerdo en las mediciones, es necesario delimitar mejor la morfología y cinemática del gas ionizado en las cercanías del núcleo.

Los nuevos datos espectroscópicos de campo integral en el *narrow field mode* con óptica adaptativa, procedentes del instrumento *Multi Unit Spectroscopic Explorer* del *Very Large Telescope*, cubren en detalle la región nuclear de la galaxia, y son usados junto con un conjunto de datos en el *wide field mode* para modelar la morfología y cinemática de múltiples líneas de emisión de gas ionizado. Se usan mapas de momentos y diagramas de posición-velocidad para describir la cinemática del gas ionizado tanto a gran escala como en el núcleo de la galaxia; el ángulo de posición y la inclinación del disco rotante se fijan utilizando el programa *Kinemetry*; también se crean cubos de datos simulados, a través de un rango de masas de agujero negro e inclinaciones del disco, para obtener el modelo de mejor ajuste, mediante la parametrización de las diferencias de los mapas de velocidad residuales (observado menos simulado).

Los resultados revelan complejidades en la cinemática del gas ionizado en el núcleo que no se habían observado en datos espectroscópicos anteriores más dispersos y superficiales: varios filamentos de gas ionizado, algunos con grandes velocidades, que pueden rastrearse hasta la esfera de influencia proyectada; un *outflow* bicónico parcialmente lleno, alineado con el chorro de la galaxia, con velocidades radiales de hasta 400 km s^{-1}; y un disco de gas ionizado en rotación, con isófotas de velocidad torcidas. La complejidad de la morfología y de la cinemática en el núcleo impiden medir con precisión la masa del agujero negro a partir del gas ionizado. Los ajustes a la inclinación del disco en las cercanías del núcleo mediante *Kinemetry*, y las estadísticas de los mapas residuales de velocidad, favorecen una masa de agujero negro de alrededor de 6.0×10^9 M$_\odot$ y un disco de inclinación de 25°, en lugar de la masa de agujero negro de 3.5×10^9 M$_\odot$ con un disco de 42° de inclinación propuestos en trabajos anteriores.

Palabras clave – dinámica de galaxias, masa de agujero negro, M87

Abstract

The black hole mass measurement of the galaxy M87, based on its stellar kinematics, is twice that determined via ionized gas kinematics, with the values disagreeing by more than 3σ. In order to gain insights into the reasons behind the disagreement between the measurements, it is needed to better constrain the morphology and kinematics of the ionized gas in the nuclear region.

The new narrow field mode with adaptive optics integral field spectroscopic data, from the Multi Unit Spectroscopic Explorer instrument on the Very Large Telescope, covers in detail the nuclear region of the galaxy, and is used with a wide field mode data set to model the morphology and kinematics of multiple ionized gas emission lines. Moment maps and position-velocity diagrams are used to describe the ionized gas kinematics in both the large-scale and the galaxy nucleus; the position angle and inclination of the rotating disk are fixed using the program *Kinemetry*; simulated data cubes, across a range of black hole masses and disk inclinations, are created to obtain the best-fit model, by the parameterization of the differences of the residual (observed minus simulated) velocity maps.

The results reveal complexities in the nuclear ionized gas kinematics not seen in earlier sparse and shallower spectroscopy: several ionized gas filaments, some with high flow velocities, which can be traced down into the projected sphere of influence; a partially filled biconical outflow, aligned with the jet, with radial velocities up to 400 km s^{-1}; and a rotating ionized gas disk, with twisted velocity isophotes. The complexity of the nuclear morphology and kinematics precludes the measurement of an accurate black hole mass from the ionized gas kinematics. The fits to the subarcsecond disk inclinations from *Kinemetry*, and the statistics from the velocity residual maps, support a high black hole mass of about 6.0 $\times 10^9$ M$_\odot$ and low inclination disk of 25°, rather than the previously proposed 3.5 $\times 10^9$ M$_\odot$ black hole mass with a 42° inclination disk.

Contents

List of Figures

Chapter 1

Introduction

There is increasing evidence that all the galaxies with a bulge component have a nuclear supermassive black hole (SMBH; e.g., Saglia et al., 2016). Direct measurements of SMBH masses - available for only 200–250 galaxies - are enabled via molecular gas (e.g., Barth et al., 2016), ionized gas (e.g., Schnorr Müller et al., 2011) and water vapor maser (e.g., Gao et al., 2017) kinematics, stellar dynamics (e.g., Rusli et al., 2011), and reverberation mapping (RM; e.g., Bentz et al., 2010).

For this relatively small and biased sample of SMBH measurements, the SMBH mass ($M_\bullet$) appears to be related to several properties of the host galaxy, such as the bulge luminosity (Kormendy and Gebhardt, 2001; Marconi and Hunt, 2003; Gültekin et al., 2009) and the bulge stellar velocity dispersion (Ferrarese and Merritt, 2000; Gültekin et al., 2009; Saglia et al., 2016). Additionally, the so-called 'single-epoch RM' method (using the width of a broad emission line and the luminosity of the nearby continuum in broad line active galactic nuclei or AGN) can be used to estimate the SMBH mass. These scaling relationships have been used to understand the role of the black holes in the formation and growth of their host galaxies (e.g., Di Matteo et al., 2005).

1.1   The galaxy M87

Measurements of a SMBH mass using different techniques can result in inconsistent results (e.g., Walsh et al., 2013; Smith et al., 2021). A notorious example is NGC 4486 (M87) where the measurement from stellar dynamics (Gebhardt et al., 2011,
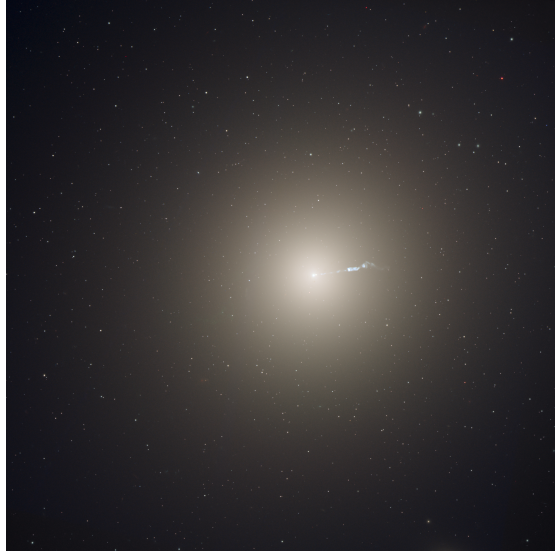
Figure 1.1.1: Galaxy M87.

hereafter G11) is twice the value from ionized gas kinematics (Walsh et al., 2013, hereafter W13), with the two values differing by more than the 3σ of each quoted measurement.

M87 (see Fig. 1.1.1[1]) is a giant elliptical galaxy located in the center of the Virgo cluster. It has a prominent relativistic jet which has been well studied on scales of 10 gravitational radii (Event Horizon Telescope Collaboration, 2019) out to ~40 kpc from the nucleus (e.g., Owen et al., 2000). The jet is projected on the sky with a position angle (PA) of 288° (Walker et al., 2018). The orientation and inclination of the nuclear ionized disk was constrained to a position angle of 45° and inclination of 42° by W13. Given this, Jeter et al. (2019) argued that the jet has an inclination of 18° to the line of sight (LOS) and found that the jet and gas disk axes are misaligned by at least 11° (with a typical misalignment of 27°).

There are several reasons to use M87 as a test case for black hole mass measurement (in)consistency from different methods: it is one of the brightest galaxies in the sky; as a massive cD elliptical with a large velocity dispersion, it is expected to host a massive $\geq 10^9$ M$_\odot$ SMBH; and it hosts one of the most studied and well-known 'radio-loud' AGN.

---

[1]https://www.nasa.gov/sites/default/files/thumbnails/image/m87-full__jpg.jpg

1.2 Measuring the SMBH mass in M87

The first attempts to measure $M_\bullet$ in M87 were made by Sargent et al. (1978) and Young et al. (1978), who suggested a black hole mass of about 10^9 $M_\odot$. In companion papers, Ford et al. (1994) presented Hα+[N II] $\lambda\lambda$6548,6583 emission-line images of the M87 nucleus using data from the WFPC2 camera aboard the *Hubble Space Telescope* (HST), and Harms et al. (1994) presented spectra at six positions in the M87 nucleus using data from the Faint Object Spectrograph aboard HST. While the nuclear emission line region was clearly not an isolated ionized disk, their isophotal fits to the emission line flux distribution in the nuclear arcsecond, the presence of trailing spiral arms, and the large emission line velocity gradients between apertures, led them to posit a nuclear ionized gas disk at PA 1°–9°, i = 42°, and a black hole mass of 2.4 × 10^9 $M_\odot$ assuming a distance of 15 Mpc to M87. Macchetto et al. (1997) used three long slit spectra from the Faint Object Camera aboard HST and found that the kinematics are best explained by a 3.2 ×10^9 $M_\odot$ black hole (for a distance of 15 Mpc and i = 51°), but noted that the disk inclination is the most uncertain parameter, with likely values between 47° and 65°.

G11 used Schwarzschild modelling of observed stellar brightness and LOS velocities to measure a black hole mass of (6.6 ± 0.4) × 10^9 $M_\odot$ for a distance of 17.9 Mpc. They used data from the Integral Field Spectrograph (NIFS) on the Gemini North Telescope with adaptive optics (AO) correction, combined with extensive kinematics out to large radii. The large scale stellar kinematics came from two sources: SAURON integral field unit (IFU) data from Emsellem et al. (2004) and VIRUS-P IFU data from Murphy et al. (2011).

W13 measured the black hole mass of M87 via the kinematics of the Hα+[N II] $\lambda\lambda$6548,6583 emission lines using data from the Space Telescope Imaging Spectrograph (STIS) aboard HST. Their spectral data were taken in five parallel slits at PA = 51°, separated by 0″1 in the plane of the sky, and with the central slit crossing the galaxy nucleus. They interpreted the ionized gas emission lines as coming from a rotating disk, with PA = 45° and i = 42°. With these parameters, and eliminating data from pixels very close to the nucleus where the Hα and [N II] lines are highly blended, they derived a $M_\bullet$ of $3.5^{+0.9}_{-0.7}$ × 10^9 $M_\odot$ for a galaxy distance of 17.9 Mpc.
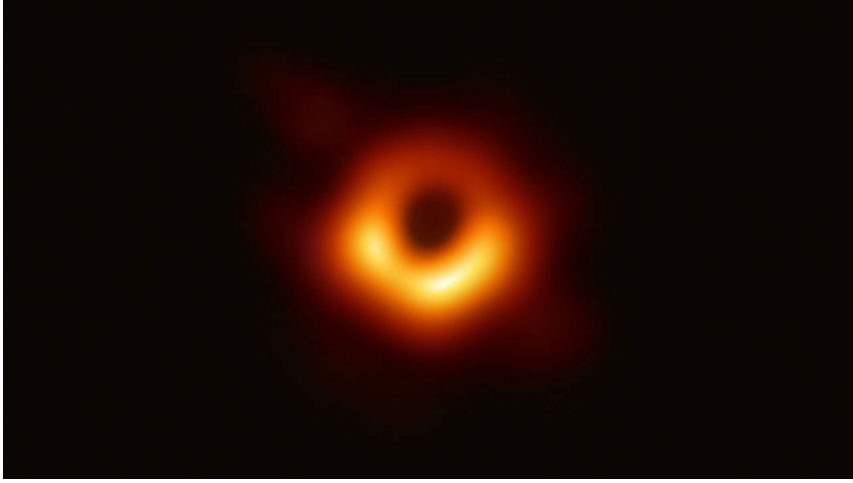
Figure 1.2.1: Ring of emission around the SMBH in M87.

Recently, the black hole mass of M87 was constrained using data from the 2017 campaign of the Event Horizon Telescope Collaboration (EHT Collaboration, 2019). A SMBH enveloped in radio emitting plasma is expected to be have a bright gravitationally lensed ring of emission surrounding the black hole 'shadow' (see Fig. 1.2.1[2]).

The diameter of ring is predicted to be $\sim$9.6–10.4 GM$_\bullet/c^2$, relatively independent of the SMBH spin (Johannsen and Psaltis, 2010; Gralla et al., 2020). The ring diameter measured by the EHT, together with standard General Relativity, imply a M$_\bullet$ of 6.5 $\pm$ 0.2 (statistic) $\pm$ 0.7 (systematic) $\times 10^9$ M$_\odot$ for a distance to the galaxy of $16.8^{+0.75}_{-0.66}$ Mpc. Scaled to this distance, the G11 and W13 SMBH masses are, respectively, $6.14^{+1.07}_{-0.62} \times 10^9$ M$_\odot$ and $3.45^{+0.85}_{-0.26} \times 10^9$ M$_\odot$ (Event Horizon Telescope Collaboration, 2019). The EHT result is thus compatible with G11 but not with W13. More recently, the EHT Collaboration used the size of the ring around the SMBH in the Galaxy (Sgr A*), together with standard General Relativity, and found an excellent agreement between the 'BH shadow' derived SMBH mass with the previous high precision (resolved) stellar dynamics mass (Event Horizon Telescope Collaboration, 2022). This latter result lends additional confidence to the EHTC derived SMBH mass of M87.

Most recently, Liepold et al. (2023) studied the stellar kinematics of M87 with data from the integral field spectroscopy at the Keck II Telescope, concluding that the galaxy is strongly triaxial (there is a misalignment of 40° between the

---

[2]https://www.science.org/content/article/images-black-hole-reveal-how-cosmic-beasts-change-over-time

kinematic axis and the photometric major axis from ∼5 kpc and outwards). They derived a SMBH mass of $5.37^{+0.37}_{-0.25} \times 10^9$ M$_\odot$ (for a galaxy distance of 16.8 Mpc), using Schwarzschild orbit modelling with a varying mass-to-light ratio (M/L).

To summarize previous SMBH mass measurements (and assuming a distance of 16.8 Mpc to M87): stellar dynamics and EHTC measurements suggest a more massive SMBH (5.4–6.5×10^9 M$_\odot$) while gas kinematics suggest a significantly lower SMBH mass: 3.5×10^9 M$_\odot$. Two immediate explanations for the discrepancy of the ionized gas kinematic value are a lower inclination for the nuclear ionized disk, and sub-Keplerian rotation of ionized gas (Jeter et al., 2019); both are explored in this work. While a full parameter space of SMBH mass 2–8×10^9 M$_\odot$ and inclination $20°$–$50°$ is explored, some pv diagrams and residual velocity maps use an illustrative 'high mass black hole' (hereafter HBH; 6×10^9 M$_\odot$), a rough mean value of the three high mass SMBH measurements) and a 'low mass black hole' (hereafter LBH; 3.5×10^9 M$_\odot$). Further, illustrative models with disk inclination i = 42° (the value derived in W13) and i = 25° are used. For example, the HBH i25 model is a HBH black hole in a disk with inclination 25°.

A more comprehensive understanding of the complexities of the ionized gas kinematics requires integral field unit (IFU) spectroscopy. Indeed, the morphology of the ionized gas in M87, on arcseconds to tens of arcseconds scales, is filamentary and complex, with evidence of multiple velocity components. The ionized gas maps of Boselli et al. (2019) show filaments extending from the nucleus up to ∼3 kpc to the NW and ∼8 kpc to the SE. They used data from the IFU Multi Unit Spectroscopic Explorer (MUSE, Bacon et al., 2010) on the *Very Large Telescope* (VLT), in its wide field mode (WFM), to model the ionized gas kinematics in the inner arcmin, and showed that the filaments have perturbed kinematics with velocity differences of $700 - 800$ km s^{-1}, but a fairly uniform velocity dispersion of ∼100 km s^{-1} over the filaments.

1.3 Constraining the ionized gas kinematics in the galaxy nucleus

To better understand the difference between the M87 SMBH masses measured using ionized gas, stellar dynamics, and EHT ring-size, new observations of M87 with MUSE in its AO narrow field mode (NFM) mode have been obtained. The

data have significantly higher spatial resolution than the WFM data used by Boselli et al. (2019) and both a higher spatial resolution and better signal-to-noise ratio (S/N) than all previous HST/STIS data. Further, unlike the data from STIS, the MUSE NFM cube fully samples the nuclear $8'' \times 8''$ region and provides a larger wavelength coverage (thus additional emission and absorption lines), and can be used to model both the stellar dynamics and ionized gas kinematics. Additionally, previous MUSE WFM observations of M87 over the central $1'$, allow constraints on the larger scale kinematics and dynamics.

The main goal of this study is to constrain the nuclear ionized gas morphology and kinematics in order to better understand the mismatch between ionized gas and stellar dynamic black hole mass measurements. It is done using WFM and NFM data, focusing on the latter. Specifically, the stellar and ionized gas kinematics are described using tools such as moment maps and pv diagrams, and the ionized gas components are presented; the position angle and inclination of the rotating disk are derived; and the model from W13 is compared with a new model proposed, through pv diagrams and residual velocity maps, to find which one fits better to the galaxy kinematics and morphology.

The document is distributed in the following sections: the theoretical framework and some basic concepts are presented in Sect. 2; the observations, data processing, software, and modelling procedure are described in Sect. 3; the results and analysis from the stellar and ionized gas kinematics are presented in Sects. 4 and 5; the discussion is covered in Sect. 6; and the conclusion is presented in Sect. 7.

Chapter 2

Theoretical framework

2.1 Supermassive black holes and its host galaxies

It is known that almost all galaxies have a supermassive black hole (SBH) at their center (Davis, 2014; Saglia et al., 2016). The masses of SBH are related with some large-scale properties of their host galaxies, such as the bulge stellar velocity dispersion (Walsh et al., 2013), the bulge luminosity or the bulge mass (Saglia et al., 2016). Those relations are known as scaling relations, and provide the empirical foundation for establishing the role of black holes in the formation and evolution of galaxies (Gebhardt et al., 2011).

The $M - \sigma$ relation is the tightest among the scaling relations (Pagotto et al., 2019). It has been studied by several authors (Ferrarese and Ford, 2005; Graham, 2008; Gültekin et al., 2009). For example, Gültekin et al. (2009) used a sample of 49 SBHMs measurements to fit the $M - \sigma$ relation. The results are shown in Figure 2.1.1.

The best fit for the $M - \sigma$ relations found by Gültekin et al. (2009) is

$$\log\left(\frac{M_{BH}}{M_\odot}\right) = (8.12 \pm 0.08) + (4.24 \pm 0.41)\log\left(\frac{\sigma_*}{200 kms^{-1}}\right), \qquad (2.1.1)$$

where M_{BH} is SBHM and σ_* is the stellar bulge velocity dispersion. The scatter of the relation was $\epsilon_0 = 0.44 \pm 0.06$.

Determining the SBHM of a galaxy is challenging. There are several methods to measure the SBHM. They differ in their model assumptions and in the dynamical
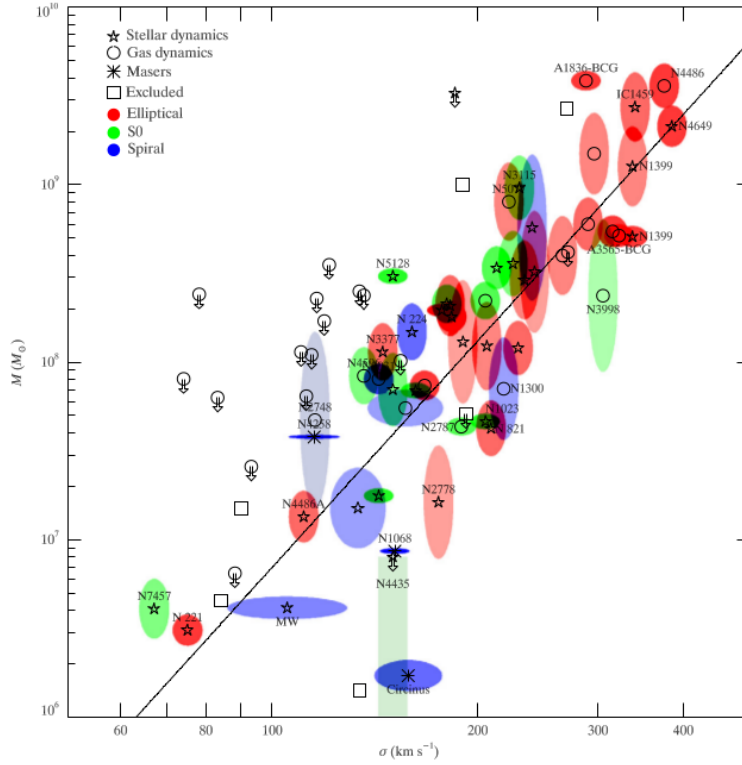
Figure 2.1.1: $M - \sigma$ relation for galaxies with dynamical measurements (Gültekin et al., 2009).

tracer used to probe the gravitational potential in the vicinity of the SBH (Thater et al., 2020). Gültekin et al. (2009) used measurements of stellar dynamics, gas dynamics and masers to fit the $M - \sigma$ relation in Figure 2.1.1.

It is not possible to use one single method across the full sample of galaxies. Moreover, when different methods are applied to measure the SBHM of a galaxy, the results are often discrepant. Therefore, the question whether the variety of methods forces an additional bias on the scaling relations arises (Thater et al., 2020).

2.2   Measurement of black hole masses

The main methods to measure SBHMs are: stellar dynamical modelling, ionized gas modelling, molecular gas modelling, water vapor maser kinematics and reverberation mapping; they are described in the following sections, focusing in the stellar and ionized gas modelling, and after presenting the concept of sphere of influence.

2.2.1 Sphere of influence of a black hole

An important length-scale for measuring the SBHM is the radius of the sphere of influence r_{SOI}. It is defined by (Smith et al., 2019)

$$r_{SOI} = \frac{GM_\bullet}{\sigma_*^2},$$

(2.2.1)

where G is the gravitational constant.

Within the sphere of influence, the motion of stars and gas is dominated by the SBH and predominantly Keplerian. Beyond the sphere of influence, the gravitational dominance of the SBH quickly vanishes (Ferrarese and Ford, 2005).

The ratio between the radius of the sphere of influence and the spatial resolution of the data is given as a rough indicator of the quality of the SBH mass estimate. All studies which have addressed the issue concluded that not resolving the sphere of influence can lead to systematic errors on the SBHM or even spurious detections (Ferrarese and Ford, 2005).

2.2.2 Ionized gas modelling

The ionized gas modelling uses the measurements of ionized gas kinematics in the environment of a SBH to determine its mass (Barth et al., 2001). This modelling is simpler than the stellar dynamical modelling because velocity dispersions are likely to be isotropic, projection effects are often small and gas disks are easy to observe even in giant elliptical galaxies with cuspy cores (Kormendy and Gebhardt, 2001).

The modelling uses the moment maps of the strongest lines in the spectra. For example, Barth et al. (2001) used the Hα and [NII] lines to model the ionized gas dynamics the galaxy NGC 3245.

In order to implement the method, a thin disk circular rotation motion of the gas is assumed. When the gas is in Keplerian motion, the model velocity field v is determined by the black hole mass, the stellar density profile and the mass-to-light ratio profile $\Upsilon(r)$ by (Barth et al., 2001)

$$v = \left(\Upsilon v_*^2 + \frac{GM_\bullet}{r} \right)^{1/2},$$

(2.2.2)

where v_* is the velocity at radius r that would result in the absence of a SBH. The model is projected onto the plane of the sky and is synthetically observed in the way that simulates as closely as possible the observations. The projection depends of the disk inclination. The SBHM is determined by finding the parameters that produce the best match to the observed velocity curves.

There are several galaxies whose SBHMs have been measured with the ionized gas dynamical modelling. In particular, Walsh et al. (2013) measured the SBHM of NGC 4486 (M87) and obtained a value of $\left(3.5^{+0.9}_{-0.7}\right) \times 10^9 M_\odot$.

Kormendy and Gebhardt (2001) show some issues associated to the ionized gas dynamical modelling. For example, most studies assume that the gas is in circular rotation. However, the gas masses are small and the gas is easily pushed around. Therefore, velocities lower or faster than circular could be seen.

2.2.2.1 Non-Keplerian models

There are models that consider the effects of non-Keplerian motion, being two of them the advection dominated accretion flow (ADAF) and the radiatively inefficient accretion flow (RIAF) (Jeter et al., 2019). These models parameterize the orbital v_r and angular v_ϕ velocities as

$$v_r = -\alpha v_{kep} \text{ and } v_\phi = \Omega v_{kep}, \tag{2.2.3}$$

where α and Ω are constants and v_{kep} is the Keplerian velocity (the same in Eq. 2.2.2). For ADAF models $\alpha \leq 0.1$ and $\Omega \leq 0.4$, whereas for RIAF models these values can be more modest (Jeter et al., 2019). Although the models does not address the physical origin of the non circular components, it provides a means to reconstruct the radial velocity profile.

The ADAF model leads to 'advection dominated' solutions, that is, when most of the viscously dissipated energy is advected radially with the flow (Narayan and Yi, 1995). On the other hand, the RIAF model occurs when the mass accretion rate at the black hole falls below 1% of the Eddington rate (Jeter et al., 2019). In this work, the RIAF model from Jeter et al. (2019) is used to consider the non circular components in the ionized gas kinematics.

2.2.3 Stellar dynamical modelling

The stellar dynamical modelling uses the stellar moment maps to estimate the SBHM of galaxies. It depends of the type of galaxy considered.

If the stars are in circular orbits, the velocity v at a radius R and a position angle ψ, both in the plane of sky, can be modeled by (Bertola et al., 1991)

$$v = v_s + \frac{AR\cos\left(\psi - \psi_0\right)\sin\theta\cos^p\theta}{\left(R^2\left[\sin^2\left(\psi - \psi_0\right) + \cos^2\theta\cos^2\left(\psi - \psi_0\right)\right] + c_0^2\cos^2\theta\right)^{p/2}}, \qquad (2.2.4)$$

where v_s is the systemic velocity, ψ_0 is the position angle of the line of nodes, θ is the inclination of the disk and A, c_0 and p are parameters to be fit. For galaxies, it is expected that $1 \leq p \leq 1.5$.

This method is useful when it is applied to spiral galaxies. Elliptical galaxies are more difficult to model (Kormendy and Gebhardt, 2001). Most luminous elliptical galaxies have little or no rotation. Therefore, it is very important to consider the velocity anisotropy. Moreover, they are expensive to observe because they have low surface brightness.

2.2.3.1 Schwarzschild method

The Schwarzschild method was developed to build dynamical models of early-type galaxies. It has been successfully applied to a large variety of density distributions, including triaxial shapes (van den Bosch et al., 2008).

The standard implementation of the method (van den Bosch et al., 2008) starts from a parameterized surface brightness distribution with a sum of Gaussians. The mass distribution is obtained by deprojecting the surface density assuming a mass-to-light ratio profile. Then, the potential distribution is calculated from the mass distribution and an assumed SBHM.

The initial conditions for a representative orbit library are found. Each orbit are integrated and the properties are stored on grids. The superposition of orbits whose properties best match the observational data is determined. Finally, the SBHM that minimize the χ^2 value is the SBHM wanted.

The Schwarzschild method has been applied to estimate the SBHM of several galaxies. In particular, Gebhardt et al. (2011) measured the SBHM of M87,

obtaining a value of $(6.6 \pm 0.4) \times 10^9 M_\odot$.

2.2.4   Other methods to measure black hole masses

In addition to the stellar dynamical modelling and ionized gas modelling, there are other methods to measure SBHMs.

The molecular gas can be used as an alternative to the stellar and ionized gas. This method use high spatial resolution measurements of the kinematics of molecular gas, available routinely with the Atacama Large Millimeter Array (ALMA). The technique has been applied to several galaxies over the past few years (Smith et al., 2019).

Spectroscopy of water-vapor maser emission from circumnuclear disks in nearby AGNs shows the kinematics of the disk (Vestergaard, 2004). Galactic water masers, which are likely the result of collisional excitation of warm interstellar gas, were first detected in 1968 and subsequently identified in a number of star forming regions and late-type stellar envelopes (Ferrarese and Ford, 2005).

The measurements of SBHMs with this method can yield high accuracy. However, this method is useful only for edge-on sources. Moreover, relatively few objects are known to have megamasers (Vestergaard, 2004).

The reverberation mapping method use the variability properties of active galactic nuclei (AGN) and quasars to measure SBHMs (Vestergaard, 2004). It uses the time delays between brightness variations in the continuum and in its broad emission lines to estimate the radius of the broad-line region. This radius together with the velocity from the full width at half maximum (FWHM), gives a measure of the SBHM (Kormendy and Gebhardt, 2001).

The method is the best and most robust method to apply to AGNs and quasars. It does not require high spatial resolution and is not affected by the nuclear glare. However, it is extremely time and resource consuming because luminous AGNs vary with smaller amplitudes and on longer time scales than lower luminous AGNs (Vestergaard, 2004).

2.2.5 Issues in the measurement of black hole masses

There are some issues associated to the SBHM measurements that should be considered. In the literature only a handful of galaxies whose SBHMs were measured through more than one method can be found. In some cases these are consistent, but in other cases there is a systematical difference between the stellar and gas dynamical black hole mass measurements (Thater et al., 2020).

For example, in relation to M87, the SBHMs measured by G11 with stellar dynamics and W13 ionized gas dynamics, are different by a factor of two, and the difference is greater than 3σ statistical uncertainty.

There are very few consistency checks between the stellar and gas dynamical methods (Gebhardt et al., 2011). Moreover, some of those studies found that gas-based methods tend to provide lower black hole masses than stellar-based methods (Thater et al., 2020). There are some possible explanations of those inconsistencies. For example, according to Thater et al. (2020), the models of ionized gas kinematics should be improved because, for example, the gas motion of massive elliptical galaxies suggest the presence of substantial random motions.

Another possibility is that the radial variation of the mass-to-light ratio along the galaxy is a source of systematic errors and hence of the difference between the methods.

2.2.5.1 Variation of the mass-to-light ratio

When the stellar or gas dynamical models are applied, the mass density profile is determined from the intrinsic light density profile through the mass-to-light ratio. This parameter is often assumed to be constant along the galaxy (Vasiliev and Valluri, 2020). However, it is possible that the mass-to-light ratio vary along the galaxy and it has an effect in the mass density profile determination (Sarzi et al., 2018).

Some work shows that SBHMs are subject to several systematic errors that have not been generally incorporated in the models used for analyzing the data. The radial variations in the mass-to-light ratio due to changes in stellar populations is mentioned as one of those systematic errors (Gebhardt et al., 2011).

In relation to M87, Sarzi et al. (2018) found that the mass-to-light ratio has a
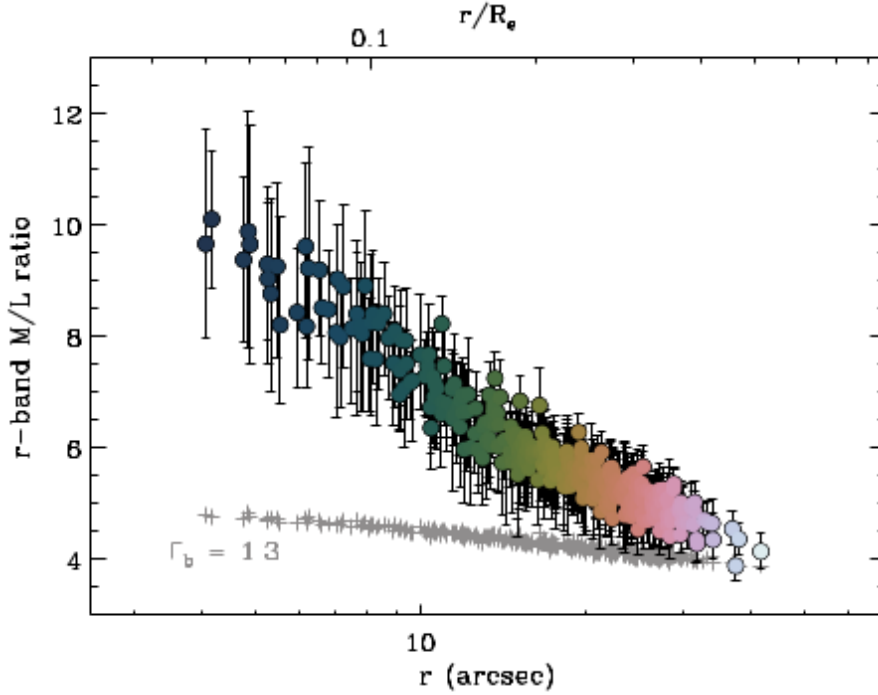
Figure 2.2.1: Radial variation of the stellar mass-to-light ratio in M87 (Sarzi et al., 2018).

radial variation, which can be seen in Figure 2.2.1. This variation ought to be included in dynamical models because there are a higher fraction of low-mass stars towards the center of the galaxy, and that has a strong impact on the projected values of the mass-to-light ratio.

It is important to mention that, in the SBHM measurements made by G11 and W13 to M87, the mass-to-light ratio was assumed to be constant along the galaxy.

The variation of the mass-to-light ratio should be considered in any part of the modelling. When the Schwarzschild model is applied, it is considered in the determination of the mass density profile through the representation of the surface brihtness distribution with a sum of Gaussians (Vasiliev and Valluri, 2020).

2.2.5.2   Data with better resolution

The data to use in the stellar and ionized gas modelling of this study will come from the WFM and the NFM of MUSE-VLT, having the data from the NFM better resolution. The use of data from a narrower field of view (FOV) but better resolutions results in an improvement of the SBHM measurements, because it leads to have information within the sphere of influence of the galaxy. On the

other hand, the data from the wider FOV shows the galaxy on a large scale and complements the data from the narrower FOV.

2.2.5.3   Inflows and outflows in a galaxy

Inflows and outflows are common in galaxies with AGNs (Schnorr-Müller et al., 2017). The presence of inflows or outflows in the galaxy affects the measurement of SBHM, since some models assume a circular motion of the gas, whereas the actual galaxy kinematics could be a mixing of circular and non circular motions, the last caused by inflows or outflows.

2.3   Galaxy kinematics

Before modelling the dynamics of a galaxy, it is necessary to have an idea of how the tracer is moving. Theoretically, it is possible if the velocity of each single particle of the tracer is known. However, measuring the velocity of the huge quantity of stars or gas molecules in a galaxy is impossible in practice.

When a galaxy or an extended object is observed, the FOV is divided in a grid of small cells or segments; it is done with an instrument called integral field unit (IFU)[1]. Each cell contains several stars or gas molecules inside, everyone with its own velocity. The signal coming from each cell is fed to a spectrograph, where its corresponding spectrum is generated; this technique is known as integral field spectroscopy (IFS). Each spectrum represents the combination of the spectra of all the stars or gas contained in the cell.

Information about the elements contained in a cell can be seen in a spectrum through the spectral lines (Carroll and Ostlie, 2007). Moreover, the velocity component parallel to our LOS can be calculated via Doppler shift, by comparing observed wavelength of one specific spectral line to the rest wavelength (when the source does not move respect to the observer).

2.3.1   Observations and data

Frequently, a camera and a spectrograph are combined to determine proprieties of galaxies or other celestial objects. When the spectrograph works in the "long

---

[1]https://www.eso.org/public/teles-instr/technology/ifu/

slit spectroscopy" mode, it takes simultaneously the spectra of several points along a slit in the space. The data is saved as a two dimensional array; the axis correspond to a specific position in the slit and a wavelength. As an example, the Space Telescope Imaging Spectrograph (STIS)[2] is an instrument in the Hubble Space Telescope (HST) that works with long slit spectroscopy (see Sect. 3.1 for more information about STIS).

It is also possible to take the spectra of several points in a two dimensional region of the space (instead a slit). The data is stored as a three dimensional array, with one spectral and two spatial dimensions. This is the case of the spectrograph MUSE[3] (see Sect. 3.1 for more information about MUSE).

W13 used data from STIS to measure the SMBH mass of M87; in this study, data from MUSE is used. In Sect. A the difference between data from STIS and MUSE (in its NFM), as well as the improvement on the quality of data in the last one, are discussed.

2.3.1.1 Active and adaptive optics

There are techniques that can be applies in order to improve the quality of the observations.

The active optics is a collection of techniques to correct slow changes in the mirror of the telescope (Morison, 2008); the changes can be due to thermal or gravitational effects. The mirror is supported by several actuators which can be moved to apply forces to the surface of the mirror, adjusting the surface profile. To know how to move the actuators, the image of a star is analysed periodically, and a computer calculated the errors in the surface of the mirror.

On the other hand, the adaptive optics (AO) compensate rapidly errors due to the turbulence in the atmosphere (Morison, 2008). This is done by monitoring the distortion of a bright star in the FOV, or an artificial reference star created by firing a laser which excites Sodium atoms in the atmosphere. The image of the distorted star is analyzed and the corrections are calculated in a computer. Due to the rate at which the corrections need to be made, they are applied to a small deformable mirror.

---

[2]https://esahubble.org/about/general/instruments/stis/
[3]https://www.eso.org/sci/facilities/develop/instruments/muse.html
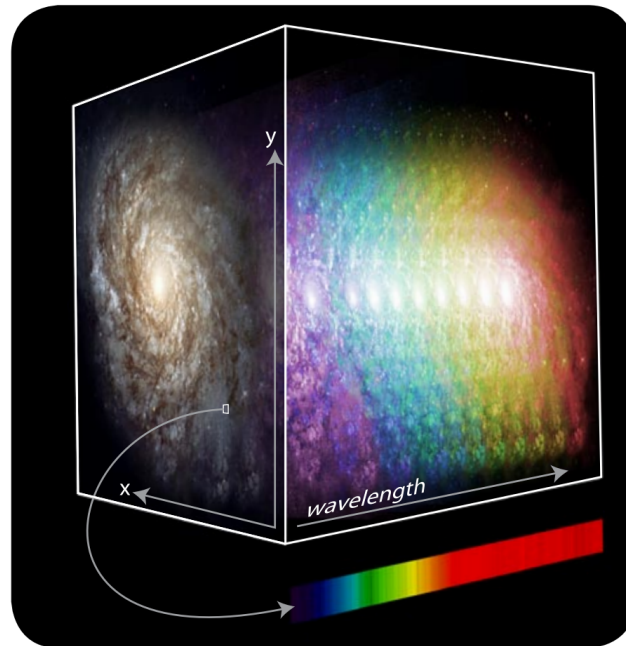
Figure 2.3.1: Representation of a data cube.

MUSE uses AO in their NFM to improve the spatial resolution of the data[4]. It is important to note that, when the creation of the artificial star is needed, the data in the Sodium wavelength range is missed.

2.3.1.2   Data cubes

As explained above, the data from the instruments of some telescopes (such as MUSE) are stored as three dimensional arrays; these arrays are called data cubes[5]. Each value in the array is called pixel, and depends on three coordinates: one spectral (that can be expressed as wavelength or frequency) and two spatial, the coordinates in the plane of the sky (see Fig. 2.3.1[6]).

If only the two spatial coordinates are considered, a pair of specific values of right ascension and declination is called spaxel. In the data cube, a spaxel is set of pixels with the same spatial coordinates, and correspond to the spectrum in the position represented by the pair.

---

[4]https://www.eso.org/sci/facilities/develop/instruments/muse.html
[5]http://astro.vaporia.com/start/datacube.html
[6]https://openresearch-repository.anu.edu.au/bitstream/1885/140441/1/ScienceWise_Vol7_No4. pdf
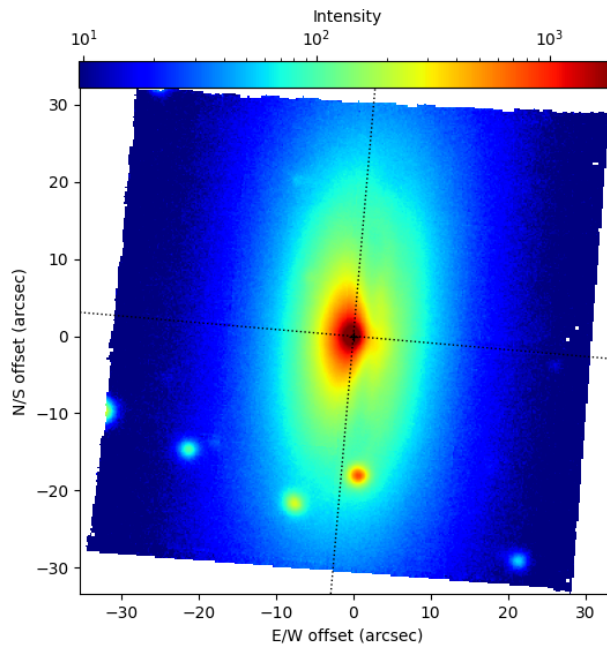
Figure 2.3.2: Stellar intensity map of the galaxy NGC4751.

2.3.2   Moment maps

Information about the kinematics of the galaxy can be obtained from data cubes; it is done by using the spectra of each spaxel to derive some quantities in that position in the plane of the sky, such as the velocity of the stars or gas. The quantities can be organized and be visualized in a map. In this study, three types of maps are specially important: the intensity, the velocity, and the velocity dispersion maps. As explained above, the velocity is the component parallel to the LOS since is calculated via Doppler shift.

The maps are also known as moment maps. A moment is done by collapsing an axis to one pixel and setting the value of that pixel to something computed from the data values along the moment axis[7]. The way of collapsing can lead to different types of moments. For example, adding all pixels along the axis gives the intensity or moment zero. The (line-of-sight) velocity or moment one is the weighted mean along the axis (expressed as velocity). The velocity dispersion correspond to the moment two.

An example of a moment map can be seen in Fig. 2.3.2; it is the intensity map

---

[7]https://casa.nrao.edu/docs/casaref/image.moments.html

of the stellar population in the galaxy NGC4751. The data cube comes from VLT-MUSE, and was done by adding all pixels along the spectral axis, in a wavelength range between 5050Å and 6000Å.

For emission lines, the moment maps are derived differently. A typical emission line has a shape that is not an horizontal line, but rather a broad line, whose shape can be represented by curves such as Gaussian or Lorentzian profiles (Hollas, 2004). The lines are broadened by different effects such as the thermal Doppler broadening, the pressure or collision broadening, or the broadening due to the Uncertainty Principle.

In this work, the emission lines are represented as Gaussian profiles

$$G(\lambda) = \frac{A}{2\pi\sigma_\lambda} \exp \frac{-(\lambda - \lambda_0)^2}{2\sigma_\lambda^2}, \tag{2.3.1}$$

where the parameters of the profiles A, λ_0, and σ_λ can be used to derive, respectively, the intensity, velocity, and velocity dispersion in each spaxel.

2.3.3   Position-velocity diagrams

A position-velocity (pv) diagram is a two dimensional extracted from a data cube. It has one spatial and one spectral dimension. The spectral dimension is the same of the data cube. The spatial dimension correspond to the positions through a slit in the FOV of the data cube. In this work, pv diagrams through curves in the FOV of the data cube are used; the curves are called pseudo-slits.

The pv diagrams can be used to compare the observed data to the prediction of a theoretical model (such as the Keplerian model); the prediction is the position-dependent projected velocity. The pv diagrams can also be compared to data from the long slit spectroscopy (such as the data from STIS).

2.3.3.1   Galaxy inflows and outflows

The velocity map from the data could have a mixing of circular and non circular motions; the non circular components are usually inflows or outflows. They are usually found by fitting a rotating disk model and subtracting it from the observed velocity field (Schnorr-Müller et al., 2017).

As explained in Sect. 2.2.2.1, models such as ADAF or RIAF also consider non

circular influences in the ionized gas flow.

2.4   M87 parameters

For clarity, the parameters for M87 used in this study are shown here. As mentioned in Sect. 1.2, the EHT Collaboration adopted a distance to M87 of 16.8 Mpc (thus a scale of 0.081 kpc per arcsecond); it also will be used in this work. G11 and W13 used a distance of 17.9 Mpc to derive their SMBH masses; these masses were scaled to the EHT distance in Event Horizon Telescope Collaboration (2019), and these updated values will be used in this work.

The heliocentric recessional velocity adopted by NED for M87 is 1284 km s^{-1} (from stars). The radial velocity listed in SIMBAD is 1256 km s^{-1}. The best fit of W13 to the ionized gas kinematics in HST/STIS data yielded a radial velocity of 1335 km s^{-1}. The fit to the stellar absorption lines in an annular radius between 2″ and 24″ in the MUSE WFM cube yields a radial velocity of 1313 km s^{-1} (see Sect. 4.1.1). The equivalent fit to the full FOV of the NFM cube yields a radial velocity of 1301 km s^{-1} (see Sect. 4.1.2). The rotational component of the diffuse ionized gas (i.e., not considering the velocity of the spiral arms) in the inner 1″ gas disk in the NFM cube is best centered using a radial velocity of 1260 km s^{-1}. In this work, unless explicitly mentioned otherwise, 'zero' radial velocities of 1313 km s^{-1} and 1260 km s^{-1} are used for the stellar and ionized gas kinematics, respectively.

Chapter 3

Methodology

3.1   Observations and data processing

Observations were made with the MUSE IFU mounted on the VLT (Bacon et al., 2010). MUSE covers a wavelength range of 4650 – 9350 with a wavelength sampling of 1.25 Åper pixel in both WFM and NFM modes. The spectral resolution is R = 3026 at 7000Å. The WFM mode has a FOV of $60'' \times 60''$, and a spatial sampling of $0\rlap{.}''2$ per pixel. The NFM mode has a FOV of $8'' \times 8''$ with a spatial sampling of $0\rlap{.}''0252$ per pixel. Since NFM data are obtained in AO mode with Sodium laser artificial guide stars, no data are obtained in the wavelength range of 5780Å–6050Å.

The WFM mode observations were made on June 28, 2014, during a MUSE Science Verification run. Data were taken at airmass 1.3, with a DIMM seeing of $0\rlap{.}''9$. The NFM mode observations were made on February 2, 2020, as part of project ID 0103.B-0581 (P.I. Nagar). Data were taken at airmasses between 1.25 and 1.5, with DIMM seeing values of $0\rlap{.}''4$ to $0\rlap{.}''5$.

The WFM data were processed with the standard MUSE pipeline (v1.6.1) and the calibrated data cubes were hosted on the ESO Archive (Processed Data Science Portal). A single processed data cube, with a total on-sky exposure time of 1800 seconds, was downloaded from this archive. The NFM data were processed by the standard MUSE pipeline (v2.8.4) and the calibrated data cubes were hosted on the same ESO Science Portal. Three processed data cubes, each with 2100 seconds of on-sky exposure, were downloaded from this archive. A fourth observation,

which was aborted after 83 seconds of exposure, was not used. The three NFM data cubes were aligned using the position of the bright nucleus and jet knots (one of the cubes had to be shifted by 2 pixels to the E and 1 pixel to the N) and combined into a single 6300 second exposure data cube. The NFM-AO mode point-spread-function (PSF) is best defined as a double Moffat function: one for the core and the other for the wings. Given that M87 is relatively northern for the VLT and has to be observed at relatively large airmass, the FWHM of the PSF core is expected to be better than 100 mas (see the MUSE *Exposure Time Calculator*[1] and MUSE User Manual[2]). With no stars in the FOV, it was not possible to measure the true PSF in the data set. However, three globular clusters in M87 can be distinguished in a continuum image of the NFM cube after subtracting a model galaxy bulge. The FWHM of the profiles of these globular clusters range between 82 and 93 mas.

The final NFM data cube provides full areal coverage of the inner $8'' \times 8''$, at a spatial resolution better than HST, a depth significantly better than the previous observations of W13, and an almost complete coverage of the optical wavelength range.

3.2   Software

In this section, there is a description of the process and programs used to obtain the stellar and ionized gas kinematics, and the models used in the analysis.

Most codes used, both publicly available and developed by the author, are in *Python*, and the 'astropy' library is extensively used. The version 3.1.0. of the *GIST Pipeline* software (Bittner et al., 2019) was used in this study, which integrates programs for deriving the stellar and ionized gas kinematics of galaxies from optical data cubes.

3.2.1   Stellar kinematics

The stellar kinematics was measured using the version of the penalized Pixel Fitting Technique (*pPXF*; Cappellari and Emsellem, 2004; Cappellari, 2017) included in the *GIST Pipeline*. The technique selects a linear combination of

---

[1]https://www.eso.org/observing/etc/bin/gen/form?INS.NAME=MUSE+INS.MODE=swspectr
[2]https://www.eso.org/sci/facilities/paranal/instruments/muse/doc.html

stellar templates which best-fit the observed galaxy spectrum and delivers stellar moment maps (total intensity, velocity, velocity dispersion, and higher moments). Before running *pPXF*, spaxels were Voronoi binned (Cappellari and Copin, 2003), setting a minimal S/N in each bin of 300 for the WFM data cube and 80 for the NFM data cube. The continuum S/N for the Voronoi binning was calculated within the wavelength range 5700Å–5750Å, and spaxels with S/N less than 3 in the continuum were excluded from the binning. Bins which included spaxels affected by emission from the jet and its knots were excluded from the analysis. The MILES stellar template library (Vazdekis et al., 2010) was also used; it covers 3525Å–7500Å and includes the Mg $\lambda5177$ and Na $\lambda5896$ lines. The *GIST Pipeline* was run on the wavelength range 5050Å–6000Å for the WFM data cube, following Sarzi et al. (2018) and Emsellem et al. (2014), and the wavelength range 5240Å-5770Å for the NFM data cube, in order to avoid the Mg $\lambda5177$ line.

Following the procedure of Sarzi et al. (2018), four moments were derived: the velocity (M1), the velocity dispersion (M2), and the third and fourth coefficients of the Gauss-Hermite polynomials, representing the skewness (M3) and kurtosis (M4) of the LOSVD. A 6th (10th) degree additive polynomial for the NFM (WFM) data cube was used. It is important to emphasize that the program provides the integrated intensity (M0) per spaxel and not per bin.

The *GIST Pipeline* includes a module to model the star formation history and derive the weighted mean of the age and metallicity of the templates used to fit the absorption lines. These are also derived via *pPXF*, but in a different run from that described above for the kinematics. Here, for both WFM and NFM data cubes, four moments were requested to be extracted and a 4th-degree multiplicative polynomial was used. The wavelength ranges were the same as used in the stellar kinematics run.

3.2.2 Ionized gas kinematics

The ionized gas kinematics was derived by fitting a single Gaussian (for the emission line) plus a first order polynomial (for the continuum) for each emission line of interest, to obtain the intensity, velocity, and velocity dispersion of the emission line in each spaxel.

Since nuclear ionized gas velocities in M87 reach almost $\sim$1000 km s^{-1}, relatively

close line complexes (e.g., Hα+[N II] $\lambda\lambda$6548,6583) are blended in the nucleus. The principle ionized gas lines were thus analyzed in groups whose wavelengths are close together. For each group, a wavelength range that covers all the lines plus continuum was selected. A straight line was fit to the continuum in order to obtain an 'emission-line only' spectrum. The intensity, velocity and dispersion maps of all the lines were obtained from a single Gaussian fit to each line in the group. In order to facilitate the fitting, two conditions were imposed: (a) all lines in a given group have the same velocity and velocity dispersion; and (b) the amplitude ratios of the following lines were fixed: [O III] λ4959/[O III] λ5007 = 0.35; [O I] λ6364/[O I] λ6300 = 0.333; and [N II] λ6548/[N II] λ6583 = 0.34.

The ionized gas kinematics can be also modelled with *GIST Pipeline* using *GANDALF* (Sarzi et al., 2006; Falcón-Barroso et al., 2006; Bittner et al., 2019). The program separates the contribution of the emission lines from the stellar absorption lines in each bin. This step is performed using the results of the *pPXF* run as inputs; for the analysis, the results from Voronoi Binning were used. The wavelength range 4750Å–6800Å was chosen for the fitting, since it covers the main emission lines in the MUSE range.

While binning improves the S/N of the spectrum and thus reliability of the resulting moment maps, spatial resolution is lost in key areas of the maps. To maintain the full intrinsic resolution of the data cube, the emission line moment maps which result from a single Gaussian fit to each spectral line in each spaxel were used.

Position-velocity (pv) diagrams were also made to reveal the full detail of the ionized gas kinematics, especially in the presence of multiple components. These are extracted from the data cubes along both straight slits and curved pseudo-slits.

3.2.3 Ionized gas modeling

In this work, the observed velocity maps and pv diagrams are compared directly to analytic kinematic models, and to simulated cubes based on analytic kinematic models. In the 'Keplerian' model, it is assumed that the ionized gas is rotating in a thin disk, with a given PA and inclination, under the influence of both the potential of the nuclear black hole and the galaxy. The rotational velocity of the gas (v_{gas}), as a function of M_{bulge}, that is, the the total mass of the stars within a

sphere of radius r centered on the nucleus, is

$$v_{gas}(r) = \sqrt{\frac{G\left[M_\bullet + M_{bulge}(r)\right]}{r}}. \tag{3.2.1}$$

For its part, M_{bulge} is derived with the following equation

$$M_{bulge}(r) = \int_0^r 4\pi r'^2 \Upsilon(r')\nu(r')dr', \tag{3.2.2}$$

where ν is the volume luminosity density of the stars, and r' is the integration variable. The V-band luminosity density of M87, as a function of radius, is taken from Fig. 1 of Gebhardt and Thomas (2009). The values in this plot were extracted with version 3.5.1. of the *Plot Digitizer Online Application*[3]. As the luminosity density profile is not an analytic function, the integral in Eq. 3.2.2 was performed numerically. Given the large black hole mass, the galaxy potential is significant only at r $\gtrsim 2''$. The radially varying M/L ratio in the V-band is taken from Liepold et al. (2023), who fit the R-band M/L variation determined by Sarzi et al. (2018) with a logistic equation, obtaining e.g. values of V-band M/L of 8.65 and 3.46 in the central and the outer part of M87, respectively.

The line-of-sight (LOS) velocity of the ionized gas in a given spaxel or along a slit was obtained by projecting v_{gas} with the following equation

$$v_{los} = v_{gas}\sin i \cos\theta, \tag{3.2.3}$$

where i is the inclination of the disk with respect to the plane of the sky, and θ is the angle (in the plane of the disk) between the major axis of the disk and the deprojected position angle of the slit.

The observables of this work are also compared to the RIAF model which Jeter et al. (2019) advanced as a potential explanation for the ionized gas derived black hole mass being lower than the stellar derived one in M87. Jeter et al. (2019) parameterized the radial and circular velocities using Eq. 2.2.3. While α and Ω in RIAF can have a range of values, in this work the specific RIAF parameters used by Jeter et al. (2019) are used: $\alpha = \sqrt{0.1}$, $\Omega = \sqrt{0.7}$, and a velocity dispersion profile $\sigma = \sqrt{f}v_{kep}$, with $f = 0.1$.

---

[3]https://plotdigitizer.com

The program *Kinemetry*[4] (Krajnović et al., 2006) is used to constrain the best fit PA and inclination of the ionized gas disk. *Kinemetry* fits the LOS velocity in concentric ellipses, and provides the best fit PA, inclination, circular velocity, and non circular velocity components for each fitted ellipse (i.e. at each radius). Velocity field fitting can be done with the PA and inclination as free or fixed parameters.

Simulated emission line MUSE cubes were created using the *KinMSpy* software (Davis et al., 2013). While this was designed to simulate molecular gas cubes, since the third axis of the cube is in velocity space, it is easily adapted to MUSE data cubes. *KinMSpy* allows the analytical rotation models to be convolved with the same spatial and spectral broadening and sampling of the observed data set. When creating a simulated emission line cube for lines from the nuclear disk, the program *skySampler* in *KinMSpy* was used to replicate the surface brightness of the emission lines; *skySampler* distributes about 2 million of simulated disk clouds in order to best fit the intensity image of the emission line. The velocity differences between the observed and simulated velocity maps are compared using several metrics and masks in order to obtain the best fit simulated cube, thus analytic model.

The 'toy' nuclear ionized outflow in Sect. 5.6 is also simulated with *KinMSpy*. This is modelled using one or two filled cones with vertices in the nucleus. The coordinate system is defined with the x axis positive to the E, the y axis positive to the N, the observer along the positive z axis, and the origin at the nucleus. The cones inclination to the observer, their opening angles, lengths, and their radial outflow velocity, were adjusted - by eye - for a good general agreement with the observed velocity maps.

---

[4]http://davor.krajnovic.org/software/

Chapter 4

Stellar and ionized gas moment maps

In this chapter, the stellar and ionized moment maps are presented. They are the main tools to describe the kinematics of the galaxy.

4.1   Stellar moment maps and properties

This study is focused in the ionized gas kinematics; however, it is worth to describe the stellar kinematics and properties, since the black hole masses obtained by using both kinematics will be compared.

4.1.1   Maps from the WFM data cube

Figures 4.1.1 and 4.1.2 are, respectively, the stellar moment maps, and the weighted mean ages and metallicities of the best-fit stellar templates, and were constructed with *pPXF* within the *GIST Pipeline* (see Sect. 3.2.1). These maps were derived using *GIST Pipeline* over a wavelength range of 5050Å–6000Å, with Voronoi binning used to obtain a $S/N \geq 300$ in each bin. All spaxels with significant jet emission were masked in the data cube to avoid confusion (except in the intensity map).

The left panel of Fig. 4.1.1 shows the stellar intensity map. The intensity is maximum in the nucleus, and decreases when increasing the nuclear distance.
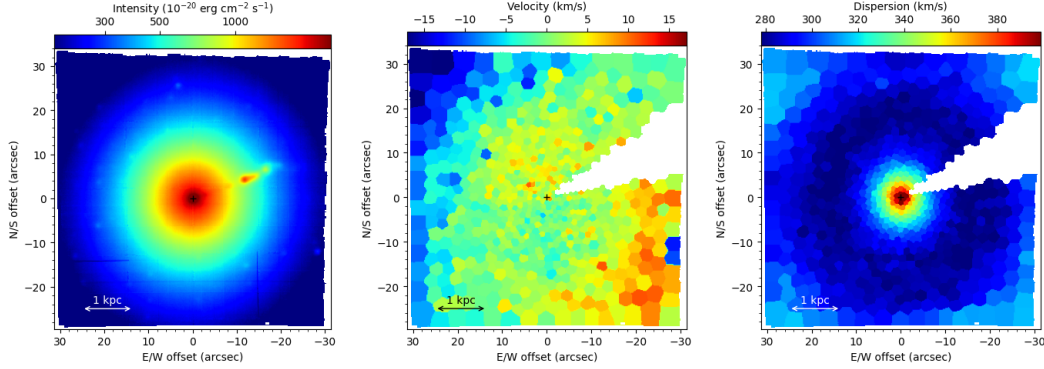
Figure 4.1.1: Stellar moment maps derived with the *GIST Pipeline* run on the MUSE WFM data cube.

The jet emission can be seen in the map; it indicates the region that needs to be masked in the other maps.

The central panel of Fig. 4.1.1 shows the stellar velocity map. A systemic (radial) velocity of 1313 km s^{-1} was used as 'zero' velocity. As seen in that map, and as earlier noted by Emsellem et al. (2014), there are two rotation patterns: one of ± 5 km s^{-1} in the inner $\sim 18''$ with redshift to the NE, and the other of ± 20 km s^{-1} (in the opposite direction, i.e. redshift to the SW) and going out to beyond the FOV of the cube. The velocity dispersion map (not shown) is symmetric with values ~ 250 km s^{-1} in a ring of nuclear radius $\sim 20''$, and steadily increasing to more than 400 km s^{-1} with decreasing nuclear distance. Given that, as expected, stellar dispersion dominates stellar rotation in the nucleus; therefore, these ± 5 km s^{-1} or ± 20 km s^{-1} of stellar rotational velocities will be ignored when modeling the gas kinematics in the next sections.

The right panel of Fig. 4.1.1 shows the velocity dispersion map. The dispersion is maximum in the nucleus, with values bigger than about 380 km s^{-1} in the inner $\sim 2''$; the values decrease from that region to reach a value of about 280 km s^{-1} at a nuclear distance of $\sim 18''$; then, the velocity dispersion increases with the distance to the nucleus.

Fig. 4.1.2 shows the maps of weighted stellar age (left panel) and metallicity (right panel) from the WFM cube. While the fitted stellar population gets older when approaching the nucleus, the stellar age and metallicity do not vary significantly out to $\sim 12''$, with values between 13–13.5 Gyr and 0.32–0.35 respectively (except in the innermost arcseconds, where the large dispersion, and the nuclear jet emission,
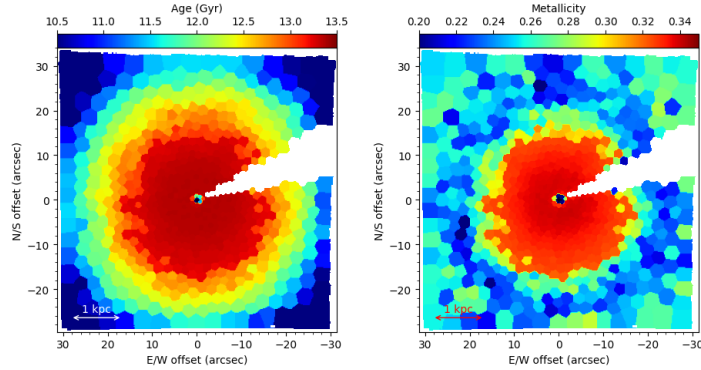
Figure 4.1.2: Maps of stellar properties derived with the *GIST Pipeline* run on the MUSE WFM data cube.

potentially confuse the fits). Outside $\sim 12''$, the stellar age decreases rapidly with increasing nuclear distance, reaching values below 10.5 Gyr. The metallicity also decreases with radial distance between $12''$ and $23''$ (values between 0.2–0.24) and then slightly increases to values between 0.24–0.3. It is worth noting the steep change in the metallicity at radius $\sim 12''$, roughly the outer radius of the counter-rotating core. For a V-band M/L ratio of 4 (as used by W13) and a G11 black hole mass, the enclosed galaxy mass equals the black hole mass at radius of about $6\rlap{.}''75$. The use of a higher V-band M/L ratio in the nucleus, following Liepold et al. (2023), still does not affect the results in the inner arcseconds of the ionized gas disk, and is mainly relevant in the analysis of the kinematics of ionized filaments at $\gtrsim 2''$.

4.1.2   Maps from the NFM data cube

Similarly of the maps in Sect. 4.1.1, the stellar moment maps of the best-fit stellar templates are shown in Figs. 4.1.3. The wavelength range to derive the map is narrower, 5050Å–5750Å, due to the use of the sodium laser in the AO. Voronoi binning, to obtain a S/N ≥ 80 in each bin, was used.

The moment maps in Fig. 4.1.3 are similar to the ones from WFM: the intensity and velocity dispersion maps decreases when moving away from the nucleus. On the other hand, the velocity map (central panel) has an irregular pattern, different from the ± 5 km s^{-1} pattern from the WFM map. A possible explanation is the difference in the S/N of spaxels in the data cubes: whereas the WFM spaxels have S/N between 40–90 in the inner $20''$, none of the NFM spaxels have S/N
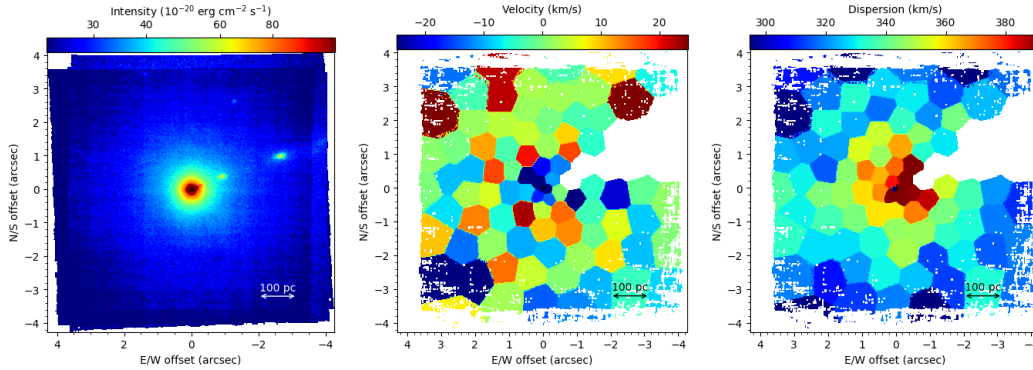
Figure 4.1.3: As Fig. 4.1.1 but for the MUSE NFM data cube.

bigger than 40; the noise is strong enough to change the ± 5 km s^{-1} pattern close to the nucleus. Another possible explanation is the absence of the sodium line in the NFM data cube, which might help in the *pPXF* fitting.

The stellar moment maps can be used to measure the SMBH mass of the galaxy. In this work, the previous black hole measurements and described in Sect. 1.2; the measurement of the SMBH using the stellar moment maps is referred to a future work.

4.2   Ionized gas moment maps

The unprecedented depth, spatial resolution, and full areal coverage of the MUSE WFM and NFM cubes reveal new complexities in the nuclear ionized gas kinematics. Since the [N II] $\lambda 6583$ emission line is the brightest in both the NFM and WFM cubes, this line is extensively used in the analysis. However, in the innermost $1\farcs5$, the emission lines are very broad and have multiple velocity components, so the Hα and [N II] lines cannot be clearly separate in the Gaussian fits. The [O I] $\lambda 6300$ emission line is used in this case, since this is a relatively isolated emission line and is bright enough to derive reliable kinematics in the inner arcseconds.

4.2.1   Hα + [N II] WFM moment maps

Ionized gas maps of the central arcmin of M87 were previously presented by Boselli et al. (2019) using the same WFM data cube used here; for these maps, a brief review of relevant known results, and discussion of features relevant to the black hole mass determination, are presented. Figure 4.2.1 shows, left to right, the total
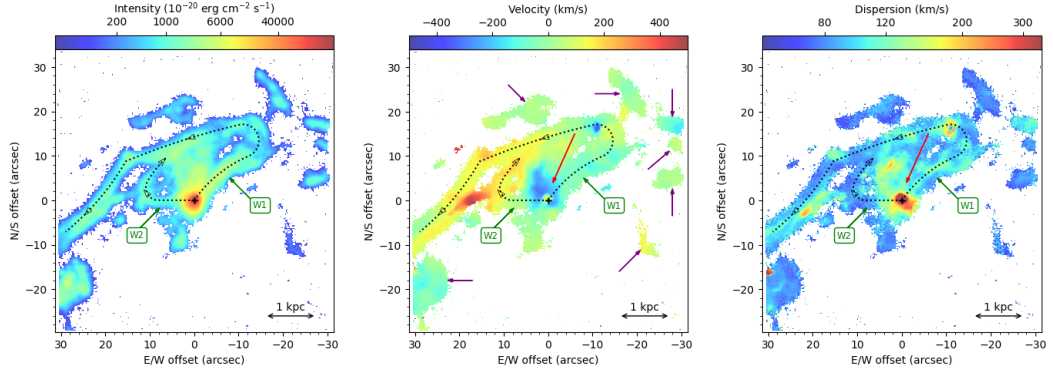
Figure 4.2.1: Moment maps of the [N II] λ6583 line as derived from Gaussian fits to the WFM data cube.

intensity, velocity, and velocity dispersion maps of [N II] λ6583 obtained from the WFM data cubes. The velocity maps assume a systemic velocity of 1260 km s^{-1}, and a sigma clipping was applied to remove bad pixels.

Several features are worth noting in these moment maps. The two black dotted lines, indicated with green arrows, trace the two primary ionized gas filaments which enter the nucleus (in projection). The filament labeled "W1" is the most prominent nuclear filament and extends beyond the WFM FOV to the W (Gavazzi et al., 2000; Werner et al., 2010; Boselli et al., 2019). The filament marked "W2" also crosses the nucleus but from the E, and connects to filament W1 about 10″ to the NE of the nucleus. There is an additional highly redshifted connection from the midpoint of filament W2 to filament W1. Additional shorter filaments and clouds, indicated in the velocity map with purple arrows, show velocities relatively different from that of filament W1. The velocity map shows a ∼6″ diameter region to the N of the nucleus (indicated with the red arrow in the velocity and dispersion maps) that is ∼200 km s^{-1} blueshifted from systemic. As explained later in this study (see Sect. 5.6), this is from a radial outflow whose axis is aligned with the jet, which adds additional complexity to the nuclear kinematics. In the innermost arcseconds one can already distinguish the posited disk-like rotating component with redshifts (blueshifts) up to ∼400 km s^{-1} to the NW (SE).

The dispersion map shows high dispersion to the NE of the nucleus; this is due to mixing rotation in the disk with the blueshifted cone of the radial outflow. The dispersion is high in a larger region to the SW of the nucleus; this is due to mixing rotation of the disk with the innermost part of filament W1 which crosses the
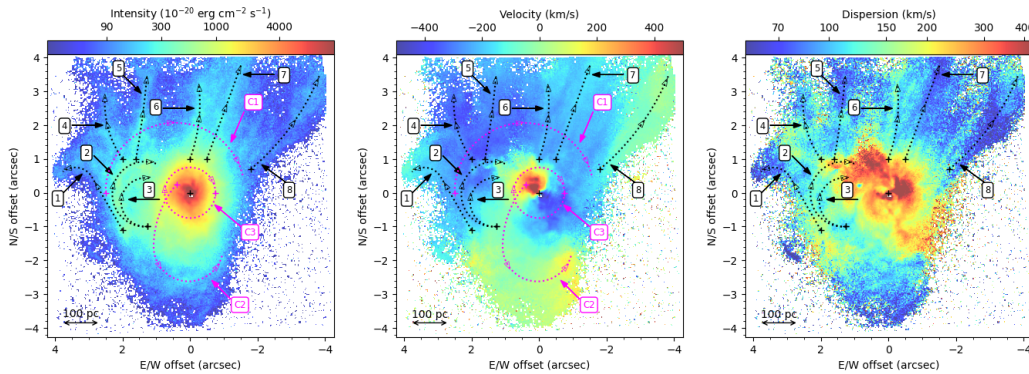
Figure 4.2.2: [N II] $\lambda6583$ emission line moment maps from Gaussian fits to the NFM cube.

nucleus in projection but maintains a blueshifted velocity, that is, the filament kinematics does not follow rotation in the potential of the black hole.

4.2.2   Hα + [N II] NFM moment maps

Equivalent NFM moment maps are presented in Fig. 4.2.2, with the locations of several pseudo-slits identified. The black dotted lines correspond to eight possible ionized gas filaments: most are easily distinguishable in at least one of the three moment maps. The three pseudo-slits shown with magenta dotted lines do not denote filaments; these pseudo-slits cross regions in the map whose velocity features help us better understand the nuclear kinematics.

The nuclear patterns seen in the WFM moment maps (Fig. 4.2.1) - the blue region to the N, the posited rotating disk, and the multiple filaments - are now resolved in exquisite detail. Given the rich complexity of the components and kinematics, these NFM moment maps will be more extensively discussed in Sects. 5.2.2 and 6. At this point, it is worth noting the diffuse and constant velocity blue- (red-) shifted emission to the N (S) of the posited rotating accretion disk which have high velocities but low dispersion, the multiple filaments to the N (with velocities apparently lower than the diffuse blue emission), and the high dispersion in the posited accretion disk. The latter is caused, in part, from the mixing of multiple velocity components: the disk and outflow (N), and the disk and a filament crossing the nucleus in projection (S).

A detailed view of the inner ionized disk as traced by the [N II] $\lambda6583$ total intensity is shown in Fig. 4.2.3. Ford et al. (1994) used isophotal fits to the inner arcsecond
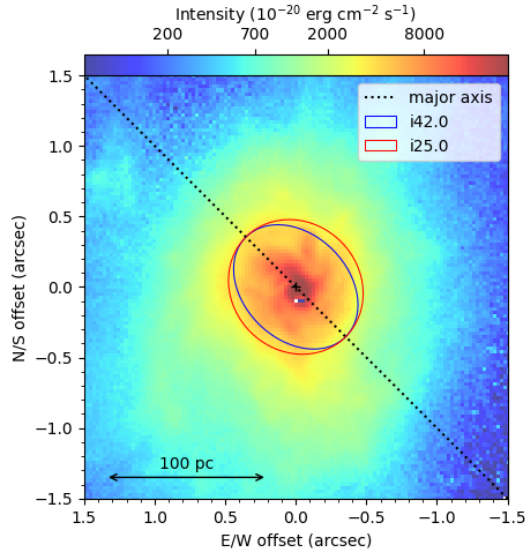
Figure 4.2.3: Zoom into the NFM moment 0 image of the [N II] $\lambda6583$ line.

ionized disk (which it is shown in this work to be a mix of different components, not only a rotating disk) to derive a PA of 1°–9° (significantly different from the kinematic PA of 40°–42° supported by all kinematic studies which allowed this PA to vary) and an inclination of 42°. Here, complex filamentary structure is still notable, and as well as some spiral arms. The most plausible explanation for these spiral arms are trailing arms in a rotating disk as noted by Ford et al. (1994). They are thus the most reliable indicator of the true extent of the disk, and thus its inclination. In Fig. 4.2.3, the blue (red) ellipse shows the expected morphology of a thin disk with inclination 42° (25°); the outer ends of the spiral arms are visually better enclosed in an i = 25° (or even lower), rather than i = 42°, inclined disk.

4.2.3 [O I] NFM moment maps

In the innermost arcseconds, the large intrinsic linewidths and the presence of multiple velocity components (especially highly blueshifted components) make the automated Gaussian fits to the Hα + [N II] lines relatively unreliable (though these multiple components are still visually distinguishable in pv diagrams). Among the other emission lines in the NFM cube, the best option is the [O I] $\lambda6300$ line as it is relatively isolated and has sufficient S/N.

Figure 4.2.4 shows the moment maps for the [O I] $\lambda6300$ line in the NFM data
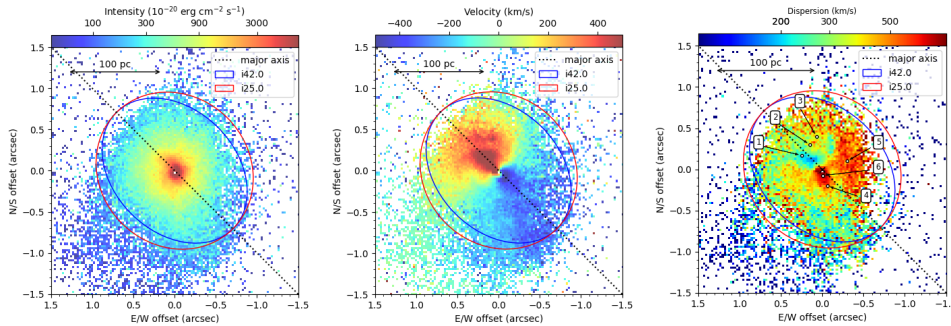
Figure 4.2.4: As in Fig. 4.2.2 but for the [O I] line in the MUSE NFM cube.

cube; the FOV is smaller here as only regions with relatively high S/N are shown. The intensity map (left panel) shows decreasing flux with increasing nuclear distance but does not clearly delineate an axisymmetric inclined disk with a clearly identifiable inclination. For reference, they are overplot, in blue and red lines, illustrative ellipses expected for a circular disk with inclination 42° (the value determined by W13) and 25° (the value favored in this work; see Sects. 5.1 and 5.5), respectively. The velocity map (central panel) shows a clear rotational pattern, but with a twist close to the nucleus, and an amplitude which is not symmetric across the minor axis; the blueshifted emission has smaller amplitudes than the redshifted emission in the radius range $0\!\!''\!1$–$0\!\!''\!3$. In the next sections, it will be explained that this is due to a filament which does not participate in rotation and crosses the disk in projection at a constant blueshifted velocity (which is not as blue as the expectation from rotation). The velocity dispersion is also non axisymmetric. In the highest S/N inner ($\leq 0\!\!''\!2$) disk, the blueshifted side of the disk has a larger velocity dispersion, reaching values of ∼600 km s^{-1}, to the SW. Spectra here are double-peaked with a red component at velocity similar to the redshifted side of the disk, and a blue rotating component (see Fig. 4.2.5). The redshifted component could be attributable to the innermost region of the biconical outflow (Sect. 5.6) or a filament crossing the nucleus in projection (Sect. 5.2.2). There is also high dispersion region $0\!\!''\!5$ to the W of the nucleus, in an area with a lower S/N. Finally, a region to the N has the lowest velocity dispersion observed (∼170 km s^{-1}), which likely traces the intrinsic dispersion of the disk (Fig. 4.2.5).

The asymmetries in the dispersion and residual velocity maps of Fig. 4.2.4 merit further details, especially given the filaments which cross the rotating disk in
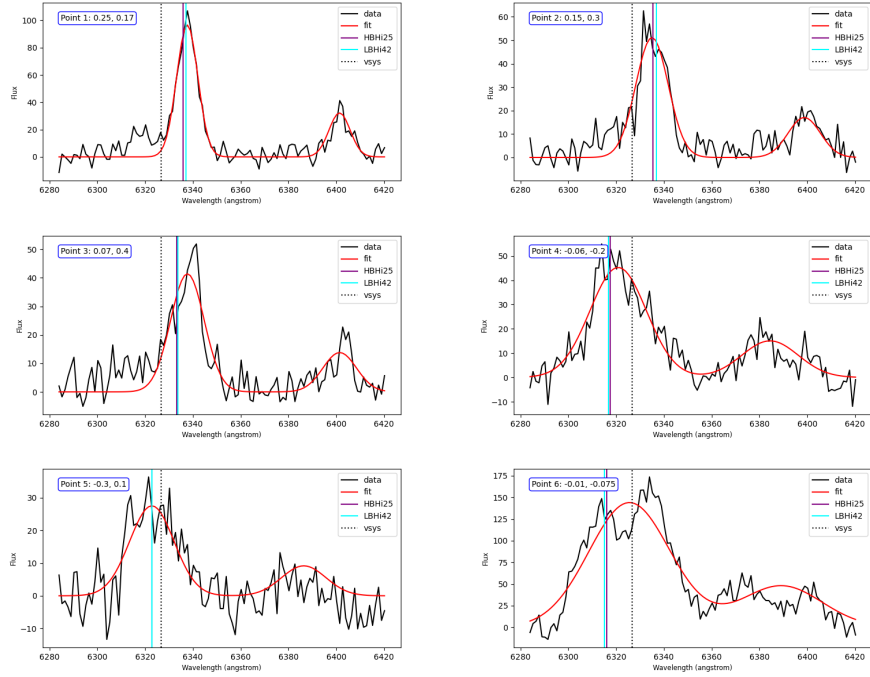
Figure 4.2.5: [O I] spectral profiles (black solid lines) in selected apertures of the nuclear ionized disk for the apertures indicated in the right panel of Figs. 4.2.4 and 5.4.2, with their single Gaussian fit overlaid (in red).

projection in the NFM FOV. The right panel of Fig. 4.2.4 show the locations of six apertures whose [O I] spectra are shown in Fig. 4.2.5; in that figure, the strong line is [O I] $\lambda 6300$ and the weaker line to the red is [O I] $\lambda 6364$; the systemic velocity (black dotted line), and rotation velocities in models with $M_\bullet = 6.0 \times 10^9$ $M_\odot$ and i = 25° (HBH i25; purple) and $M_\bullet = 3.5 \times 10^9$ $M_\odot$ and i = 42° (LBH i42; cyan) are overplotted. Apertures are labeled by their number and their RA and Dec offset from the kinematic center in arcseconds.

Apertures 1 and 3 are in the 'spiral arms' seen in the residual velocity maps (a subtraction of a velocity model from the velocity map; see Fig. 5.4.2), while aperture 2 is in a region between them. As seen in these three spectra, the central velocity of the best fit single Gaussian coincides with the peak velocity of the spectrum, confirming that the velocity map from Gaussian fitting reproduces well the central velocity of the strongest emission component. However, all three apertures show a potential weaker (and well separated) component near about 6320Å. This weak blueshifted component is at the expected velocity of the posited blue conical outflow to the NE (Sect. 5.6). Aperture 1 is in the region of the lowest velocity dispersion of the nuclear ionized disk. It is clean, and at high S/N,

fit with a single Gaussian with dispersion $\sim$170 km s^{-1}. This value likely reflects the true dispersion of the disk in the absence of additional non-rotating velocity components. Apertures 4, 5, and 6 are in regions of high velocity dispersion. Aperture 4 seems to have a single component with high dispersion and a redshifted velocity with respect to the predictions of both HBH i25 and LBH i42 models; it is possible that they are a blend of two components with approximately the same intensity. The double component nature is most clearly seen in the spectrum of aperture 6: here a rotating component is distinguishable from a redshifted component: 950 km s^{-1} from the rotating component and $\sim$350 km s^{-1} from systemic; this velocity offset would be expected if the gas were in the red cone of the nuclear outflow (Sect. 5.6). Aperture 5 (W of the nucleus) also has high velocity dispersion, but the S/N here makes it impossible to tell if it is formed from one or more components. Overall, apart from small velocity offsets from models, regions of the disk show higher velocity dispersion due to additional components, and should be masked when comparing observed velocities to simulated rotating model cubes. Specifically, the high velocity dispersion regions and/or the spiral arm feature regions are masked in Sect. 5.4.

Chapter 5

Ionized gas modeling

In this chapter, the different components of the ionized gas kinematics are explored in more detail. Models for the rotating component, as well as an approximation to the ouflow component, are also presented and discussed.

5.1 Ionized disk geometry: Position angle and inclination

In this section, the best fit PA and inclination of the ionized gas disk are determined using *Kinemetry* (see Sect. 3.2.3). Three different velocity maps were independently input to *Kinemetry*: the velocity maps from the single Gaussian fitting of [O I] and of Hα + [N II], and also a directly 'collapsed' [O I] velocity map. The directly 'collapsed' velocity map is a moment 1 map of the [O I] $\lambda6300$ line, created with the *spectral-cube* package in python, which only included a limited wavelength (thus velocity range): to avoid contamination from the weaker [O I] $\lambda6364$ line (63 Å or 3000 km s^{-1} redward in restframe), at each spaxel, only a range of ±40Å (or about ±1900km s^{-1}), centered on the wavelength predicted by the HBH i25 rotational model for that spaxel, was included.

In the first run, for each velocity map, both PA and inclination were free parameters: the best-fit results are shown in the top two panels of Fig. 5.1.1. In the case of PA, all three input velocity maps give relatively similar results: the PA starts at value between $58°$ and $64°$ at $0\rlap{.}''1$, decreases out to radius $0\rlap{.}''4$, and increases beyond this radius. The kinematic analysis further below concentrates on radii
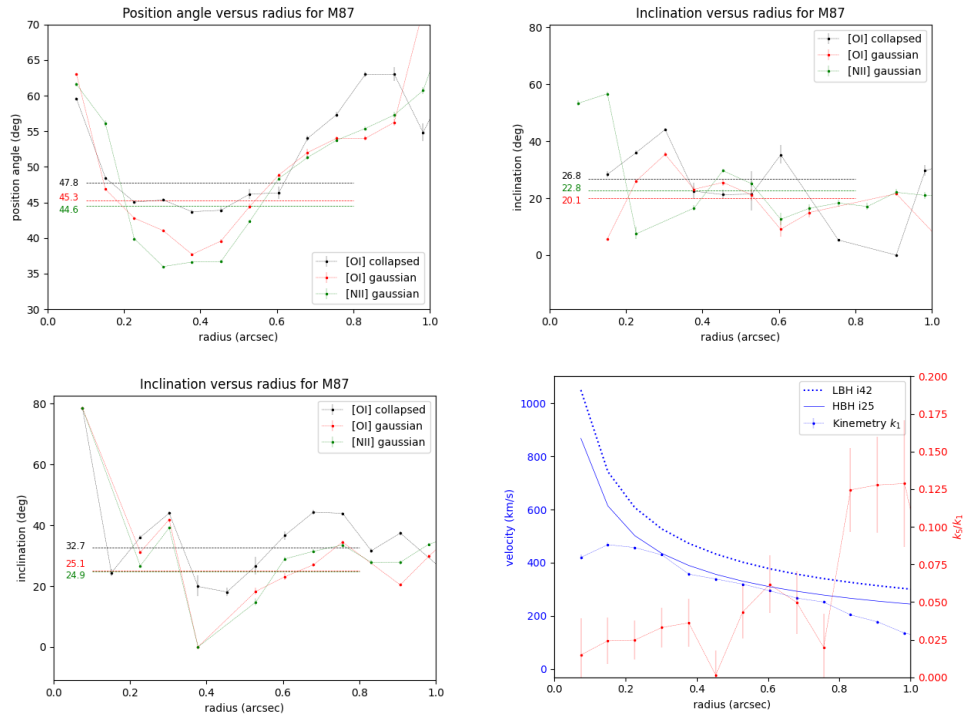
Figure 5.1.1: Results from *Kinemetry* for the sub-arcsecond ionized gas velocity maps.

between 0″.1 to 0″.8: in the inner 0″.1 the lines become broad and blended and velocity isophotes are twisted; farther than 0″.8 the S/N of disk ionized gas is low and other components (outflow and filaments) dominate. In Fig. 5.1.1, the horizontal lines in the corresponding color show the mean value over radii between between 0″.1 and 0″.8. While only the 'collapsed' [O I] velocity field shows a PA more or less constant over a large part of this useful radius range, the mean PA over this radius range is close to 45° for all three velocity fields. The top left panel of Fig. 5.1.1 shows the equivalent results for the best fit inclination. None of the velocity fields give a constant inclination with radius, and the inclination evolution appears to be relatively chaotic with values between 0° and 45°. The mean inclination values between 0″.1 and 0″.8 shown are between 17° and 24° for the three velocity maps.

Given the results of the first run of *Kinemetry* (and the value previously derived by W13), a PA of 45° was fixed and only the inclination was left as a free parameter in the second run of *Kinemetry*. The bottom left panel of Fig. 5.1.1 shows the result of these runs. The variation of inclination with radius is now slightly less chaotic than in the first run but still varies between 20° and 45°, when it is not 0°. The

mean values over the 0.″1–0.″8 range are remain between 17° and 24°, except for the 'collapsed' [O I] map, which has a higher mean value of 33°. The bottom right panel shows the rotation curve (i.e. the k_1 parameter from *Kinemetry*; connected blue dots) and compares this to expectations of Keplerian rotation for the HBH i25 (solid blue line) and LBH i42 (dotted blue line) models, all following the left hand y axis. The red line, following the right hand y axis shows the k_5/k_1 ratio (i.e. non-circular velocity to circular velocity ratio) derived by *Kinemetry*: low values here imply that disk velocities are dominated by rotation.

While these *Kinemetry* results do not concretely point to a disk inclination close to 25°, they provide an additional indication that inclination values closer to 20°–25° are more plausible than 42°. It is also an indication of the relatively complex gas motions in the disk could preclude an accurate measurement of the black hole mass.

5.2   Ionized gas filaments

In this subsection the kinematics of the ionized gas filaments seen in the outer (WFM) and nuclear (NFM) regions are presented and discussed. Evidence indicating that each has its own flow velocity, and only some are affected by the SMBH potential, while others cross the nucleus only in projection, will be presented, meaning that the nuclear 'gas disk' is not an isolated relaxed and well-ordered rotating disk, but a mix of gas rotating in a 'disk', emission from gas in filaments, some of which enter with their own proper bulk velocity, and some of which only cross the nucleus in projection. Further below, the extra complexity of disentangling the nuclear biconical outflow is also discussed.

5.2.1   Wide field mode filaments

In Sect. 4.2.1, two large-scale filaments in the WFM moment maps (Fig. 4.2.1) were highlighted. The pv diagrams of the [N II] emission line along these filaments are shown in Fig. 5.2.1, together with the predictions of disk rotation in the potential of the SMBH and the galaxy under different assumptions of black hole mass and disk inclination. Since the apertures are curved, they are referred as pseudo-slits. The offsets (x-axis) in the pv diagrams start at the position of the nucleus, and continue along the dashed lines shown in Fig. 4.2.1. That is,
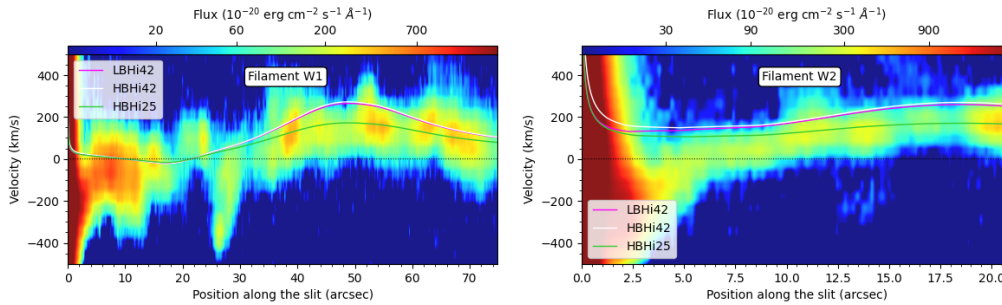
Figure 5.2.1: Position-velocity diagrams of the [N II] λ6583 line for pseudo-slits along the gas filaments W1 and W2 identified in Fig. 4.2.1.

the x-axis value indicates the distance traveled along the line from the nucleus (indicated with a black cross in Fig. 5.2.1) and not the radial distance from the nucleus. The colored solid lines in the pv diagrams denote the velocities expected from gas in a rotating thin disk for the following models: LBH i42 (magenta), HBH i42 (white), and HBH i25 (green).

All of these models have a disk at PA = 45°. The galaxy potential is obtained as described in Sect. 3.2.3, and becomes significant only at radii beyond 2″. The LBH i42 and HBH i42 (magenta and white) models use the inclination and position angle found by W13 for the ionized gas disk. The green line is illustrative for a HBH and a disk with the lower inclination suggested by the data (see Sect. 5.3).

Filament W1 is the longest and most prominent. None of the velocity models follow the observed velocities in the first 14″. The filament leaves the nucleus at PA roughly close to the minor axis of the W13-posited gas disk and one would expect relatively small Keplerian velocities. Nevertheless, velocities are between ± 100 km s^{-1} (with an extreme value of ~ 400 km s^{-1}) over the first $\sim 30''$ of the filament. Between 20″ and 30″ there are two - potentially bubble-shaped - clouds at 90 km s^{-1} and -350 km s^{-1}. The latter has a velocity highly different from the rest of the filament and the models; this bubble is either not part of the filament (but in the same LOS) or caused by a kink or instability in the filament. From 36″ onward, the observed velocities follow the overall pattern expected from the HBH i25 rotating disk model in both values and shape. To make the HBH i42 and LBH i42 models agree with the observed velocities over this range, one would require to change the ionized gas 'zero' velocity by ~ 80 km s^{-1} to the blue, which would imply an even greater difference between the recessional velocities of ionized gas and stars (~ 1300 km s^{-1}).

Filament W2 is shorter and shows relatively smooth velocity changes along its length, with a relatively low dispersion (compared to filament W1) at offsets larger than $3''$. Similar to filament W1, the observed velocities close to the nucleus are systematically bluer than all the rotating disk models, especially in the first $5''$. Once more, at distances larger than $10''$ the HBH i25 model most closely fits the data in values and shape. It is also interesting to note that filament 2 appears to (at least in projection) connect to filament W1 through an additional highly redshifted bridge to the E of the nucleus (Fig. 4.2.1), though there is no explanation for this velocity pattern.

Except in the innermost $5''$–$12''$, the observed pv diagrams of both filaments W1 and W2 are well explained - in velocity and velocity gradients - by circular rotation of gas in a disk with inclination close to $25°$ (green line in the pv diagrams). At these large radii, the galaxy potential, rather than SMBH mass, drives the circular velocity. This is clearly illustrated by the fact that the HBH i42 (white lines) and LBH i42 (magenta lines) models result in very similar velocity predictions. The disk inclination is thus the dominant parameter, and the degeneracy between black hole mass and inclination when fitting the kinematics of the inner arcseconds of the ionized gas disk is no longer cause for concern.

5.2.2 Narrow field mode filaments

In this part, the eight filaments and the pseudo-slits identified on the higher resolution NFM moment maps (Fig. 4.2.2) are described. The pv diagrams of the [N II] $\lambda6583$ line along these filaments and pseudo-slits are shown in Figs. 5.2.2 and 5.2.3. As previously explained, the x-axis of these figures are offsets along a curved slit, and not the radial distance from the nucleus. Most of the filaments are to the north of the nucleus, and cross the highly blueshifted region. The pseudo-slits (magenta lines in Fig. 4.2.2) do not follow gas filaments, but their pv diagrams are useful to understand the complex nuclear kinematics, so they are also presented here.

Each of the eight filaments in Fig. 5.2.2 can be differentiated from the others in at least one of the three moment maps in Fig. 4.2.2. Significant effects of the black hole potential on the ionized gas as getting closer to the nucleus are expected to be seen, especially in the inner few arcseconds. However, the filament pv diagrams are almost all significantly different from all of the model predictions of thin disk
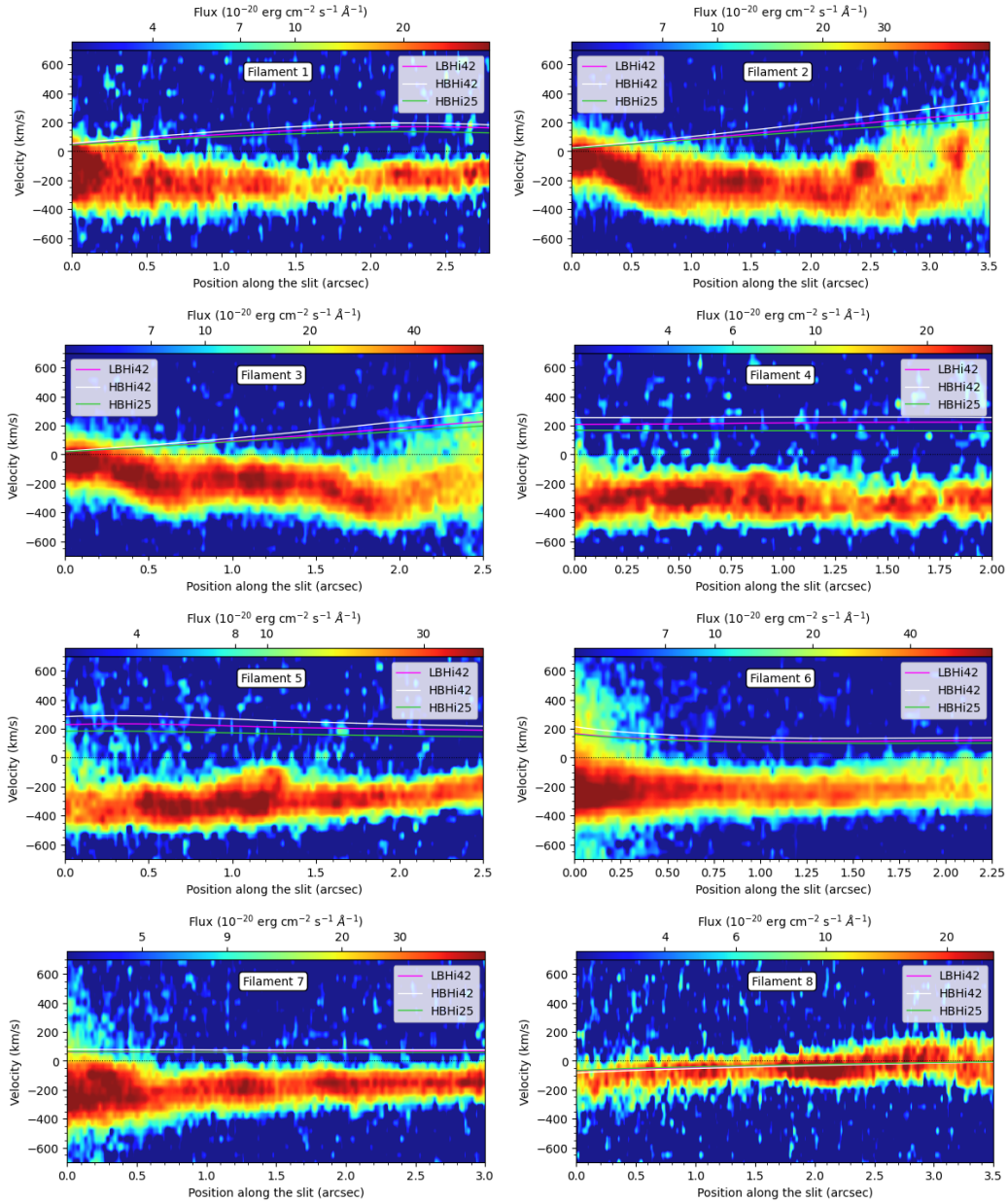
Figure 5.2.2: As in Fig. 5.2.1 but for the eight filaments marked with black dotted curves in the NFM moment maps of Fig. 4.2.2.
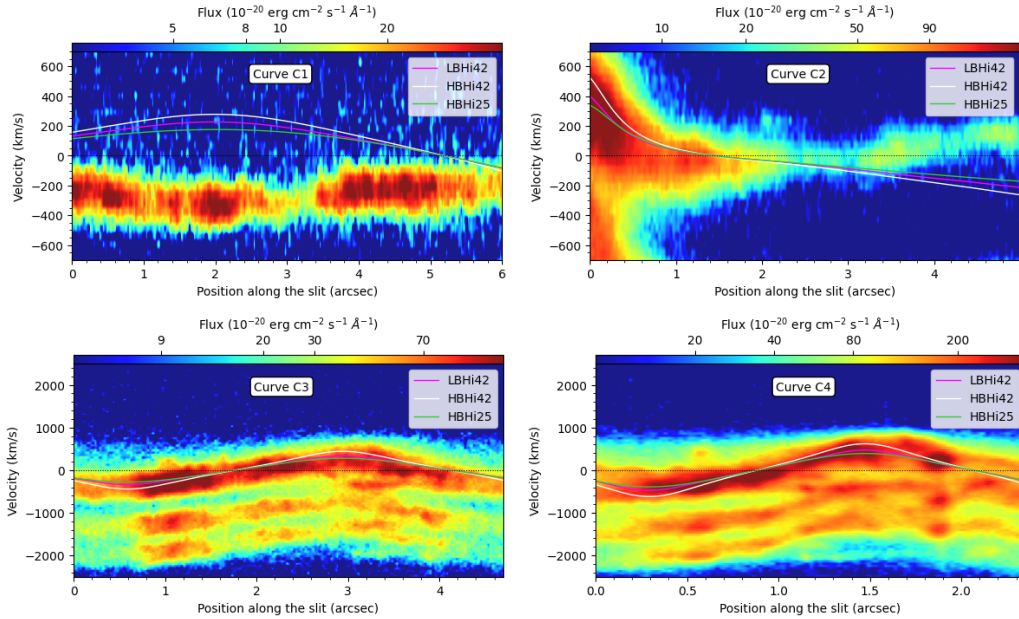
Figure 5.2.3: As in Fig. 5.2.1 but for pseudo-slits C1, C2, and C3 marked in magenta dotted curves in the moment maps of Fig. 4.2.2, and an extra pseudo-slit at a nuclear radius of 0″.375.

rotation in the black hole and galaxy potential. Only filament 8, which is to the W of the highly blueshifted region (see middle panel of Fig. 4.2.2) approximately follows the rotating disk model predictions.

Filament 1 can be distinguished in the intensity map; its pv diagram shows differences of up to ~400 km s^{-1} blueward from the rotation model predictions. Filaments 2 and 3 have a semicircular form in the moment maps, with their extremes closest to the nucleus. Both can be distinguished in the intensity map, with filament 2 also partially distinguishable in the velocity and velocity dispersion maps. For both filaments, the disagreement between observed velocities and the rotational models increases with increasing nuclear distance. The disagreement is nevertheless smaller close to the nucleus than the case of filament 1. Filaments 4 and 5, clearly distinguishable in the intensity maps, are in the highly blueshifted zone to the NE of the nucleus. They are the most blueshifted filaments in the inner nucleus, with blueshifts of about 250–350 km s^{-1} from systemic, and more than 500 km s^{-1} offset from the rotation model predictions. Nevertheless, their dispersion velocities are ≤150 km s^{-1} and both appear to have only a single velocity component. Filaments 6 and 7 are distinguishable in the intensity and velocity maps. With velocities between −200 km s^{-1} and −150 km s^{-1}, they are

less blueshifted than filaments 4 and 5. Filament 6 shows a higher dispersion ($\sim$200 km s^{-1}) than filaments 4, 5 and 7. Filaments 4 to 7 in the NFM can also be distinguished in the WFM maps: at the lower resolution of WFM, they are distinguishable as three filaments (or one filament and a loop).

Filament 8, the westernmost filament, is clearly distinguished in the intensity and velocity map. It is the only filament to approximately follow the rotating disk models, though it is slightly more blueshifted than the models at offsets of 0''.1–0''.2 and 1''.8–2''.2. Its dispersion is also small ($\leq$150 km s^{-1}). Given its velocity and morphology, it is likely the inner region of filament W1 of the WFM (Fig. 4.2.1).

Overall, filaments 1 to 7 follow individual flow velocities which cannot be explained by a rotating thin disk. Only filament 8 approximately follows the expectations of a rotating thin disk, but since this filament approaches the nucleus in a PA close to the minor axis of the disk, it cannot be used to constrain the black hole mass.

The following discussion is for the pv diagrams (Fig. 5.2.3) of the pseudo-slits C1 to C3 in the NFM cube (dotted magenta curves in Fig. 4.2.2). The pseudo-slit C1 (top left panel of Fig. 5.2.3) cuts through most of the northern filaments from east to west while maintaining a roughly constant radial distance from the nucleus. Nevertheless its pv diagram shows a constant blueshift of $\sim$200 km s^{-1} from systemic except over offsets of 1''–3'' along the pseudo-slit (effectively the NE region) where a constant blueshift of $\sim$300 km s^{-1} is seen. While this is visible in the velocity map, the pv diagram emphasizes the relatively uniform velocity of the northern filaments, the uniformly small dispersion velocity, and the lack of additional velocity components. Effectively the filaments are bright concentrations embedded within, and sharing the velocity of the more diffuse blueshifted emission region. The observed velocities are even further blueshifted from the rotation model predictions, and in fact appear as a rough mirror image of these.

The pseudo-slit C2 starts in the redshifted side of the inner disk, travels to the SE along a small filament (see left panel of Fig. 4.2.2) and then crosses the redshifted ionized gas to the south in the NFM moment map. In its pv diagram (top right panel of Fig. 5.2.3), the high dispersion can be noted in the first arcseconds, as well as the fact that the kinematics roughly follow the LBH i42 and HBH i25 rotating disk models in the inner two arcseconds. A small velocity discontinuity at 2''.5–3'' offset along the pseudo-slit can be seen, which delineates the separation

point between the rotating (inner) and non rotating (outer) components of the gas. However, the continuity of the velocity transition from one component to the other indicates interaction between the two components.

The pseudo-slit C3 is a circle with radius $0\rlap{.}''75$ centered on the nucleus. The x axis starts (offset = 0) W of the nucleus and moves clockwise. Over all of the pseudo-slit except the NW quadrant the observed velocities are well fit with either the LBH i42 model, or a HBH i25 model. In the NW quadrant, the observed velocities are systematically $\sim$200 km s^{-1} blueshifted from the model predictions. While filaments 6 and 7 of the NFM can be seen as separate components at even larger blueshifts, the $\sim$200 km s^{-1} blueshift in the NW does not appear to be an additional component but rather a warp or systematic bulk velocity in the disk. At this radius, the S (especially the SW) section of the disk appears the least confused with additional components or velocity offsets.

The pv diagram shown in the bottom right panel of Fig. 5.2.3 is for a circular slit like C3, but at half its radius (now r = $0\rlap{.}''375$). Here, the disk velocities are more symmetric in all PAs, with the LBH i42 and the HBH i25 both providing a reasonable fit. The N blueshifted filaments are still clearly distinguishable. At this smaller radius, the gas to the SW shows a second velocity component: a non-rotating component $\sim$300 km s^{-1} blueshifted from systemic velocity. This component dominates the rotating component at smaller radii, and is the primary reason why the blueshifted side of the rotating disk shows smaller absolute velocities than the redshifted side of the disk over radii $0\rlap{.}''1$–$0\rlap{.}''3$. The velocity of this non-rotating component matches that of filaments 6 and 7 as they approach the nucleus in projection.

5.3 Position-velocity diagrams compared to analytic models

Figure 5.3.1 shows the pv diagrams of the Hα+[N II] $\lambda\lambda$6548,6583 line along nuclear slits in, left to right, PA = 45° (the W13-based disk major axis) and 135° (disk minor axis) in the WFM cube. Even at this relatively low spatial resolution, and at large nuclear offsets, the complex kinematics and presence of multiple components can be seen. The inner 3″–4″ to the NE shows highly blueshifted (instead of redshifted) emission, which, with increasing radius smoothly transitions
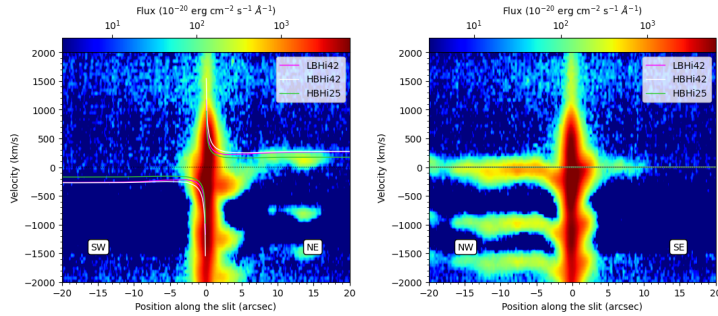
Figure 5.3.1: PV diagrams of the Hα+[N II] λλ6548,6583 lines in the WFM cube along the W13 major and minor axes.
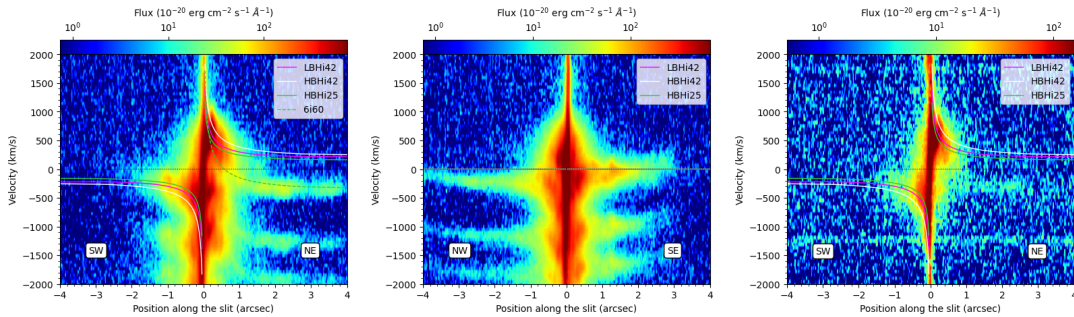
Figure 5.3.2: PV diagrams of the Hα+[N II] λλ6548,6583 and [O I] emission lines in the NFM cube, along the W13 major and minor axes.

to systemic velocity. Further, at 8″–16″, the bright emission line gas does not follow rotation in a disk with 42° inclination. Along the minor axis to the NW, the nuclear gas is also blueshifted, and other kinematic 'wiggles' are seen further away from the nucleus. Figure 5.3.2 shows the equivalent pv diagrams in the NFM cube (left and middle panels) together with the pv diagram of the [O I] λ6300 line along a nuclear slit at PA = 45°. In the left panel, the gas 1″.5–4″ to the NE of the nucleus (positive offsets in the figure) primarily traces the kinematics of the filaments and outflow, and there is no clear sign of rotating gas at these offsets. When the nuclear offset decreases below 1″.5, instead of continuing 'into' (in projection) the nucleus at the same bulk velocity offset, the gas velocity gets redder very rapidly but smoothly (crossing systemic velocity at 0″.8 in projection) and then further increases until it is indistinguishable from gas in the rotating disk. Adding a simple bulk (systemic) blueshift to the rotation models cannot reproduce this velocity pattern (the observed velocities drop too rapidly with increasing nuclear distance). A filament crossing the nucleus only in projection would also not explain this pattern, as the projected nuclear separation is always

larger than the true 3 dimensional nuclear distance. For illustration, the dotted green line shows the predictions of gas rotating around a G11 black hole, but at an inclination of 60° and with a bulk blueshift of 650 km s^{-1}. A possible explanation for this feature is that nuclear gas, initially feeding the black hole in a plane with a larger inclination than the main disk, is entrained into the blue cone of the conical outflow (see Sect. 5.6).

Comparing the observed pv data to the models, the HBH i42 overpredicts the observed velocities, while both the LBH i42 and the HBH i25 models are relatively indistinguishable when compared to the data. Along the minor axis (central panel of Fig. 5.3.2), the blueshifted gas to the NW is clearly visible at an almost constant ∼200 km s^{-1} blueshifted velocity. The [O I] pv diagram (right panel of Fig. 5.3.2) covers a smaller range of offsets. Here the HBH i42 model is clearly in the upper envelope of the observed velocities.

All WFM and NFM pv diagrams clearly show filaments nearing the nucleus (in projection) but not following rotational kinematics of the black hole. In several cases, multiple velocity components are seen, so that single Gaussian fits are not usable here. While the highly blueshifted components can be disentangled in pv diagrams at most PAs, for reasons of brevity they are not shown here. To avoid some of the confusion created by the highly blueshifted filaments, the [O I] λ6300 emission line is used instead, which, while weaker, is relatively isolated from other emission and absorption lines, and is detected out to ∼1″ radius (right panel of Fig. 5.3.2).

5.4   Residual velocity maps

The results of the *Kinemetry* (Sect. 5.1) and residual (observed minus simulated) velocity map analysis (Sect. 5.5) support low inclinations for the ionized gas disk. To better visualize the differences when using low and high inclination disks, and to discern residual velocity features after rotation velocity subtraction, this section presents the residual (observed minus model) velocity maps of competing rotational models. The model velocity maps used in this section are created using *KinMSpy*.

It is important to note that the RIAF model includes a radial outflow in the disk plane, which results in an observed kinematic PA which is offset from the
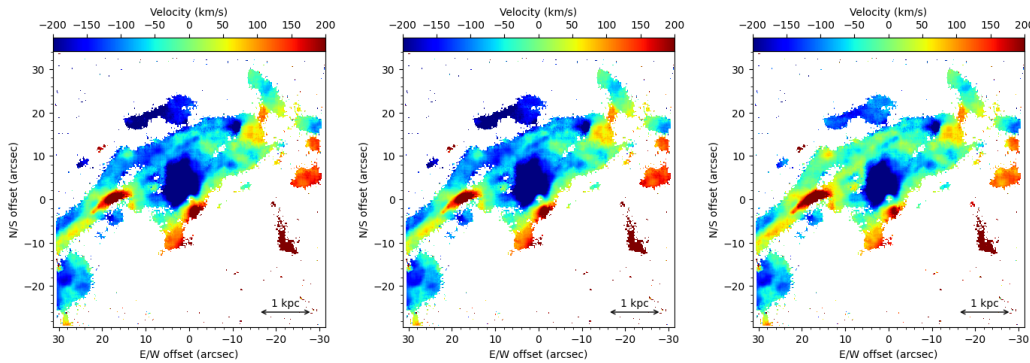
Figure 5.4.1: Residual velocity maps of the [N II] $\lambda6583$ line in the data cube.

rotational kinematic PA. For this specific RIAF used here, a rotation with major axis at PA = 27°, added to the outflow component, results in an overall observed kinematic PA of 45°. Alternatively, if the near and far side of the disk were exchanged, then a rotation PA of 63° would give the same result.

Fig. 5.4.1 show the residual velocity maps of the [N II] $\lambda6583$ line after subtracting the LBH i42, HBH i42, and HBH i25 models. At the relatively large nuclear distances seen in the WFM, the galaxy potential dominates the black hole potential, thus avoiding the degeneracy between inclination and black hole mass in the inner arcseconds. Both the HBH i42 and LBH i42 models (i.e. both models with i = 42°) oversubtract the velocities seen over most of the filaments W1 and W2. The i = 25° model however produces a velocity residual closer to zero. Here it is important to note that a recession velocity of 1260 km s^{-1} is used, the velocity which best fits the inner ionized gas disk, and which is 75 km s^{-1} bluer than the value used by W13. With the recessional velocity of 1260 km s^{-1}, the observed velocity fields of filament W2 (and a large part of filament W1) of the WFM are primarily at velocities between systemic and 180 km s^{-1} (redshifted). As discussed in Sect. 5.2.1, reducing the velocity residuals of the i = 42° models requires using a smaller recessional velocity, which would be even further away from the stellar recessional velocity, and thus more unlikely to be correct. In any case, except for some prominent kinks and bubbles in filament W1, and extreme redshifts in the apparent bridge between the W1 and W2 filaments, both W1 and W2 appear to be primarily composed of gas in a rotating (and partially filled) ionized gas disk. The large blue region $1''$–$10''$ N of the nucleus, and the smaller red region $\sim2''$ S of the nucleus, seen in the residual maps can be explained by the biconical outflow (Sect. 5.6).
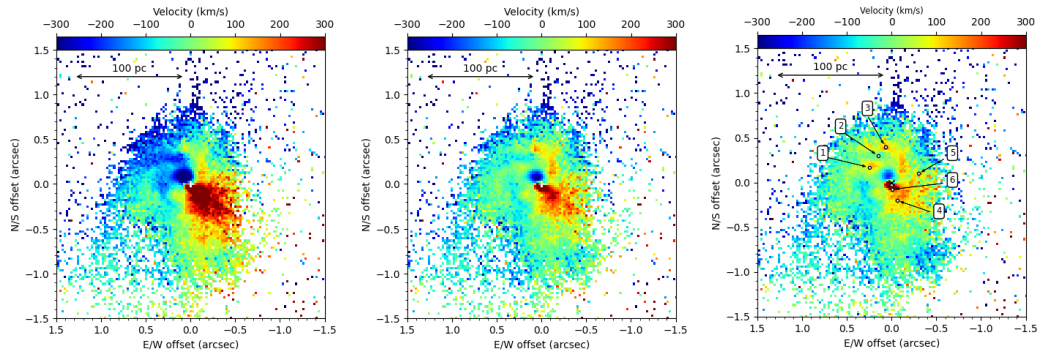
Figure 5.4.2: As in Fig. 5.4.1 but for the [O I] line in the MUSE NFM cube.

Residual velocity maps for the [O I] line are shown in Fig. 5.4.2: left to right are
the residuals after subtracting the HBH i42, LBH i42 and HBH i25 models. The
HBH i42 significantly over predicts the LOS observed velocity field. The LBH i42
and HBH i25 models give roughly similar residuals, though the latter provides
velocity residuals closest to zero.

The twisted ionized gas velocity isophotes in the innermost 0″.1 (most clearly
discerned in Fig. 5.4.2, but also clear on close inspection of Fig. 4.2.2) is an
important result of this work. At a radius of 0″.3, the PA of the disk appears to be
∼45° as found by W13 and *Kinemetry* (see Sect. 5.1). By ∼0″.1 the PA appears
closer to 90°. In the innermost pixels the PA appears to twist even more. This
innermost twist is best visualized in the residual velocity map (right panel of Fig.
5.4.2). Here the residual map implies a rotation major axis of ∼18°, which is
perpendicular to the PA of the inner jet of M87, as would be expected if the jet
was launched perpendicular to the accretion disk. Alternatively, this relatively
N-S inner velocity gradient could trace the bases of the biconical outflow discussed
in the Sect. 5.6. Macchetto et al. (1997) previously noted the velocity field twist
inside 0″.2 when modeling their HST spectra with thin disk models. The twist
in the apparent PA appears to continue outside the radius of 0″.3, as supported
by the results in Sect. 5.1. However, at even larger radii, as shown earlier in
this section, the velocity field of the filaments in the WFM maps at r ∼10s of
arcseconds can still be fit well with a rotating disk at PA ∼45° and inclination
25°.

Emsellem et al. (2014) have shown that the stellar velocity field in the central
∼15″ of M87 is twisted, with the stellar kinematic PA changing rapidly from

17° to −124°. In the innermost ∼5″, the stars rotate with a major axis close to PA = 20°, with the NE side redshifted. This pattern can also be seen in the WFM stellar map (Fig. 4.2.1), where visually the inner ∼10″ stellar kinematics support a PA of 30°–45°, with the NE receding, i.e., similar to the pattern seen in the ionized gas here. The main difference is that the stellar rotation velocity amplitudes are relatively low ($\lesssim$20 km s^{-1}) and that the twisted isophotes are seen on much larger scales.

The other important feature to note in the HBH i25 residual velocity map of Fig. 5.4.2 is a three or four armed spiral pattern at ∼100 km s^{-1} redshift, embedded in a blue (outflow or filaments) halo. This velocity-traced spiral arm pattern closely matches the spiral arm pattern noted by Ford et al. (1994) in their HST ionized gas maps, and seen clearly in the moment 0 maps (e.g., Fig. 4.2.3). The spiral pattern is reminiscent of the ionized gas spirals around Sgr A*, which extend out to ∼3 pc, and appear to trace Keplerian circular or elliptical orbits around Sgr A* (Zhao et al., 2009).

5.5 Constraining black hole mass and inclination

In order to obtain a best fit model (in black hole mass and disk inclination) to the nuclear 'Keplerian' rotating ionized gas disk seen in the NFM cubes, the program *KinMSpy* was used to construct simulated data cubes of the [O I] line in the inner 1″, for a range of black hole masses (2×10^9 M$_\odot$ to 8×10^9 M$_\odot$ in steps of 0.5×10^9 M$_\odot$) and disk inclinations (20° to 50° in steps of 2°). In all models, the disk PA was fixed at 45°, and the same galaxy potential was used.

As described in Sect. 3.2.3, *KinMSpy* was given the intrinsic spatial and spectral resolution of MUSE, the pixel sampling of the MUSE cubes, and clouds were placed to best reproduce the respective moment 0 image of the emission line, in order to make the most realistic simulated cubes. Velocity fields of these simulated cubes were then created in python using the *spectral-cube* package. The residual (observed minus simulated) velocity map was then used with several masking schemes and several metrics, to determine the simulated velocity map which best fits the observed velocity map.

As emphasized in several previous sections, both the nuclear ionized disk and the large scale ionized gas emission show complex kinematics, often due to the
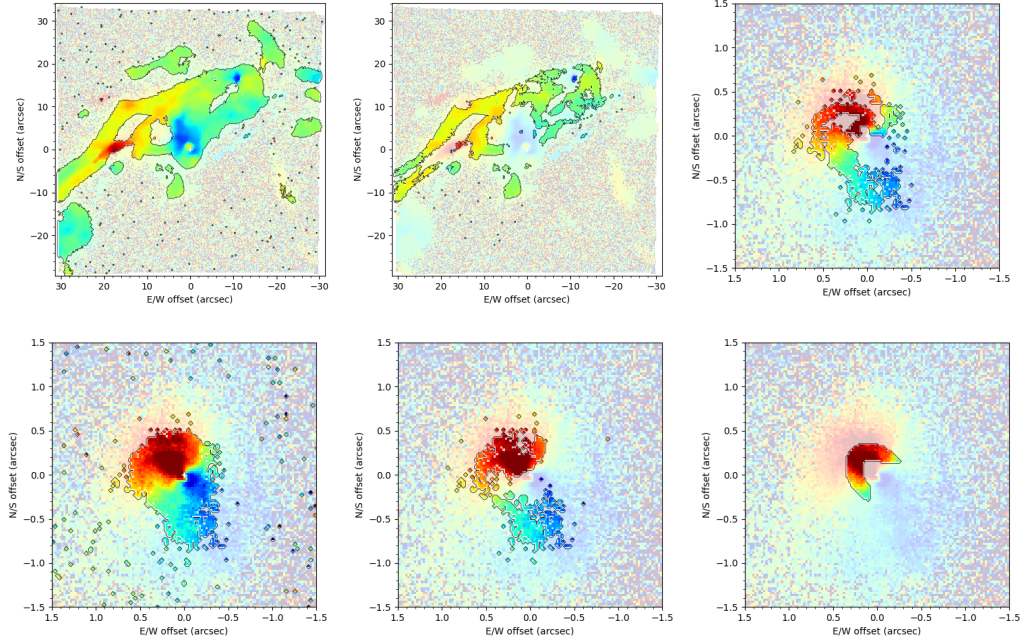
Figure 5.5.1: Masks applied to the subtracted velocity maps.

superposition of several distinct components. The masking used on the residual velocity field before calculating best-fit metrics is thus important. Several masks were used (see Fig. 5.5.1):

- Gauss-fit mask: all spaxels which show large residuals between the observed spectrum and the best fit Gaussian were masked. This effectively masked both spaxels with low S/N and with complex profiles which could not be fit with a single Gaussian (left panels in Fig. 5.5.1: Hα+[N II] $\lambda\lambda$6548,6583 at the top and [O I] λ6300 at the bottom).

- Sigma-clip mask: all pixels in which the dispersion map has values larger than 350 km s^{-1} were masked. This masks also effectively avoids the inclusion of spaxels with multiple velocity components (central panels in Fig. 5.5.1: Hα+[N II] $\lambda\lambda$6548,6583 at the top and [O I] λ6300 at the bottom).

- Spiral-arm mask: all pixels which fall within the mini spiral arms seen in the [O I] velocity residual map for the HBH i25 model (right panel of Fig. 5.4.2) were masked, specifically pixels with absolute residual velocities larger than 100 km s^{-1} (top right panel in Fig. 5.5.1).

- Annular mask: all pixels outside the annular region between 0$''$.2 and 0$''$.4 from the nucleus, and pixels inside a rectangular region between −0$''$.6 and
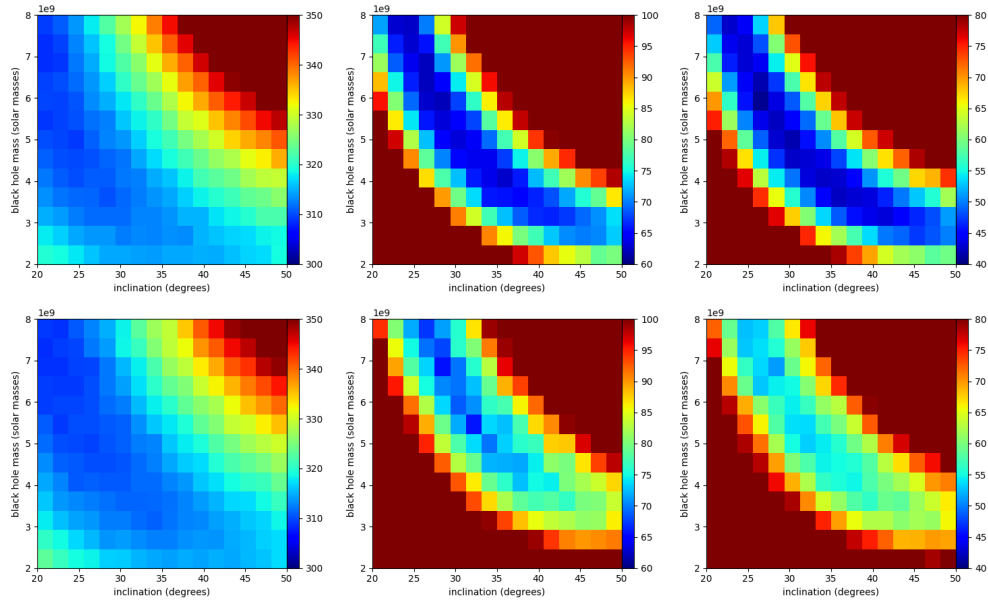
Figure 5.5.2: Standard deviation (in km s^{-1}) of values in the residual velocity map, as function of the black hole mass and disk inclination of the model.

0″.1 in E/W offset, and −0″.45 and 0″.15 in N/S offset, were masked. This mask retains the highest S/N regions of the disk while deleting the innermost region (with isophotal twists) and the high velocity dispersion nuclear region (bottom right panel in Fig. 5.5.1).

At each value of SMBH mass and inclination, several metrics from the masked velocity residual (observed minus simulated) map were calculated; multiple metrics were used in order to be robust against changes in the histogram profile and average velocity in a given residual map. These included the standard deviation, the mean of the absolute difference, the difference between the 84 and 16 percentiles, and the r squared value. These metrics were then evaluated across the parameter space of SMBH mass and inclination. Most combinations of masks and metrics deliver similar results with respect to favored pairs of SMBH mass and disk inclination, so only selected examples are shown here. The exercise above was also made for a comparison of the observed [O I] velocity map with simulated cubes of the RIAF model of Jeter et al. (2019, see Sect. 3.2.3).

Figure 5.5.2 presents the resulting metric obtained from the [O I] emission line residual velocity maps for a Keplerian rotation model (top panels) and for the Jeter RIAF model (bottom panels). Specifically, here the results of the standard deviation of the residual velocity maps for three different masks are shown (left to

right): Gauss-fit, sigma-clip, and spiral-arm.

Focusing on the top panels in Fig. 5.5.2, i.e., 'Keplerian rotation' models, in general, the minimum values of standard deviation follow a 'banana' pattern, with almost equal support for high black hole masses at low inclinations as for low black hole masses at higher inclinations, with black hole mass decreasing with increasing inclination. The left panel is the result from the Gauss-fit mask. It favors a high black hole mass and small inclination, with a minimum beyond the range of the plot; the masking here does not necessarily exclude all high dispersion regions and spiral arms seen in the moment (and residual) maps. The sigma-clip and spiral-arm masks (central and right panels) yield similar results. Both plots show a banana-shaped dark blue region of minimum values, where the metric does not vary significantly. For the specific LBH and HBH values, the inclinations at minimum standard deviation are, respectively, $\sim 37°$ and $\sim 28°$. There is very slight support for an HBH at lower inclination: the standard deviations (for the sigma-clip mask) for the LBH with i = 37° and HBH with i = 28° are 62.2 and 64.8 respectively, a difference of 4.2%; for the spiral-arm mask, the difference is 3.92%, in the same sense. In general, over most masks and metrics, a HBH at low inclination is favored over a LBH at high inclination only at the 4% level.

The equivalent results for the RIAF model residuals are shown in the bottom panels of Fig. 5.5.2. As with the Keplerian model, a dark blue banana-shaped minimum region is seen, but this is offset with respect to the Keplerian results as expected: sub-Keplerian rotation results in higher inclinations favored for a given black hole mass. Nevertheless, the level of sub-Keplerian rotation in this specific RIAF model is not sufficient to support the scenario of a HBH at inclination 42°: values of Ω significantly lower than $\sqrt{0.7}$ would be required. Once more the Gauss-fit mask (left panel) favors a high black hole mass and low inclination beyond the plot. For the sigma-clip and spiral-arm masks, the inclination ranges for a minimum standard deviation for the LBH and HBH are, respectively, 40°–43° and 30°–31°. The respective standard deviations are 76.5 and 68.7 for the sigma-clip mask, and 56.4 and 54.4 for the spiral-arm mask. The standard deviation for the HBH case is thus lower by 11% for the sigma-clip mask and 4% for the spiral-arm mask. Thus overall, within the Jeter RIAF model, a HBH in a low inclination disk provides a slightly better fit than an LBH in a higher inclination disk, and a HBH in a disk with inclination i = 42° is not supported.
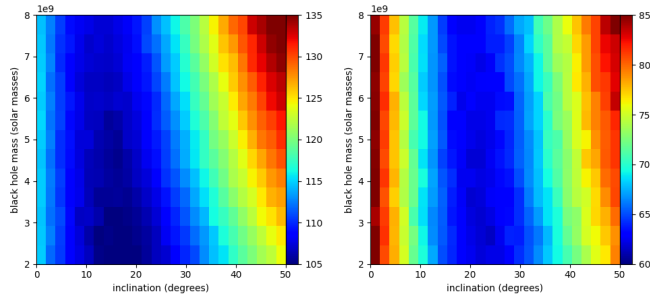
Figure 5.5.3: As Fig. 5.5.2 but for the WFM Hα+[N II] $\lambda\lambda$6548,6583 velocity map and the 'Keplerian' rotation model.

Comparing 'Keplerian disk' scenarios with the Jeter RIAF scenario, the following is noted: (a) for a HBH, the 'Keplerian disk' scenario gives lower velocity residuals than the RIAF model across all masks and metrics; (b) interestingly, a LBH in a i = 42° disk is better supported in a RIAF scenario as compared to the 'Keplerian disk' scenario, and larger values of Ω would make the RIAF model even more favorable.

The same exercise was made for the velocity map of the large scale filaments seen in the WFM cube, and the Gaussian-fit and Sigma-clip masks explained for [O I]. Here, the velocity map of the Hα + [N II] line created via Gaussian fitting was used (with a single Gaussian fit to each of the Hα and [N II] lines). The only differences from the process above is that (a) the inclination between 0° to 50° was varied; (b) the sigma-clip mask was created by masking pixels with velocity dispersion above 100 km s^{-1}; and (c) only the 'Keplerian' rotation models were used. The resulting standard deviation in the residual velocity map, for intensity masking (left) and velocity dispersion masking (right) are shown in Fig. 5.5.3. In both cases, the minima are seen at relatively small inclinations, almost independent of the black hole mass. This is since most of the non-masked area is outside of the sphere of influence of the SMBH. The minimum standard deviation is seen at an inclination of about 18° for the Gauss-fit mask and 24° for the sigma-clip mask; using the other metrics and masks give similar results. This supports the scenario that the filaments are rotating in a disk with inclination ~20°, close to the value supported for the inner sub-arcsecond disk in this study.
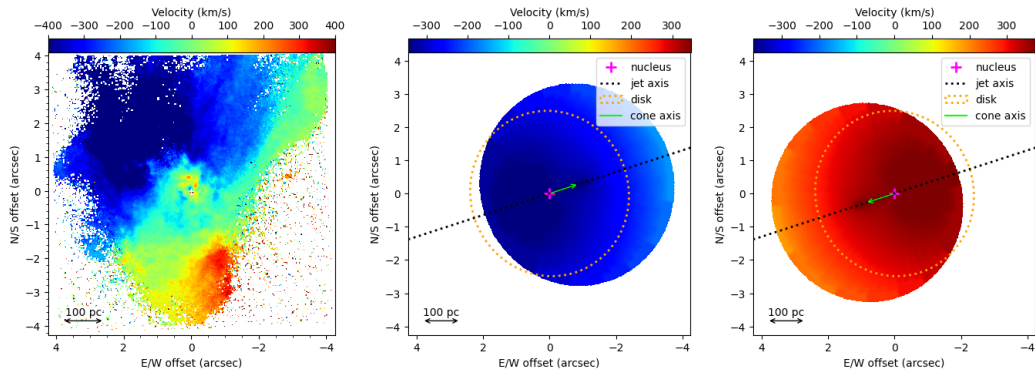
Figure 5.6.1: Residual [N II] velocity map and models of a filled conical outflow made with *KinMSpy* with each cone showed separately

5.6   Ionized gas outflow

The moment maps and pv diagrams in the diffuse blue region and filaments to the N of the nucleus clearly demonstrate the presence of a non-rotating component. Additionally, some excessively redshifted gas is seen about 3″ SW of the nucleus. With projected velocities up to 400 km s^{-1}, the most viable explanation for these velocities is an AGN driven outflow.

The left panel of Fig. 5.6.1 shows the residual velocity map (observed velocity minus the HBH i25 rotating disk model) of the [N II] $\lambda6583$ line, and emphasizes better not only the blue and redshifted regions to the N and S, respectively, but also the velocity gradients seen in these.

One could attempt to reproduce these velocity features with a (fully-filled) biconical outflow. Illustrative examples of these are shown in Fig. 5.6.2, where the cone axes were chosen to illustratively 'match' the blueshifted and redshifted regions, or to project onto the PA of the jet. there, the left panel illustrates a geometry which allows blueshifts to the N and redshifts to the S, as seen in the left panel of Fig. 5.6.1. The axes of the cones in this case project to PA 10°, roughly perpendicular to the jet axis. The right panel illustrates the case in which the cone axis is aligned with the jet axis, i.e. at PA −72°. Neither of these illustrative models can satisfy the observed velocities while maintaining an origin in an AGN produced outflow along the axis of the jet.

Instead biconical outflow is proposed, in which the cones are only partially filled with ionized gas; a scenario supported by the filamentary and patchy nature of
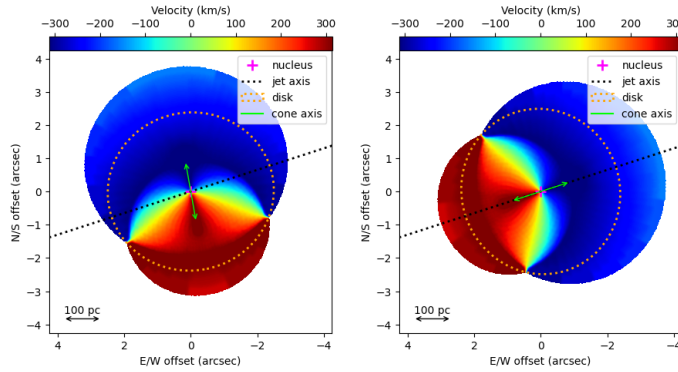
Figure 5.6.2: As in the middle and right panels of Fig. 5.6.1 but with both cones superimposed in a single panel.

the ionized gas in the inner 30″. To illustrate this scenario, Fig. 5.6.1 shows the velocity structure of each cone individually. Here both cones have the same opening angle (45°), and their orientation is chosen so that both cone axes project to PA −72° (the PA of the jet). The velocity gradients in each bicone match those seen in the residual velocity map (left panel of Fig. 5.6.1). Thus, supported by the non-axisymmetric filamentary and patchy ionized gas seen on scales larger than 1″ in both the NFM and WFM cubes, it can be posited that the diffuse and filamentary ionized gas to the N (outside the accretion disk and within the NFM FOV) is primarily between the nucleus and the observer, and the ionized gas to the SW of the nucleus (outside the accretion disk and within the NFM FOV) is behind the nucleus from the observers point of view. This partial filling of the approaching and receding cones then well recreates the velocity residual map of Fig. 5.6.1. This posited partially filled biconical outflow could also explain two other ionized gas blobs to the S and SE beyond the NFM FOV, but observed in the WFM FOV residual velocity map (bottom right panel of Fig. 4.2.1).

Chapter 6

Discussion

The full areal coverage of the nuclear (new deep MUSE-AO NFM cube) and larger scale (archival MUSE WFM cube) ionized gas, allows improved constraints on the morphology and kinematics of the ionized gas in the inner $0\rlap{.}{''}1$ to $30''$ in M87. On the larger scales, filaments W1 and W2 (which are 10s of arcseconds in extent) show velocities which can, in most of their extent, be fit with a partially filled gas disk in inclination i ∼25° rotating in the potential of the galaxy. Nevertheless, certain sections of these filaments show large kinks and highly dispersive velocities. The W arm of W1 appears to cross the nucleus in projection, and at relatively low rotation-corrected velocity. While it cannot be clearly traced between $1''$–$2''$ W of the nucleus, its incoming direction aligns with a high velocity residual (after rotation correction) region in the SW quadrant of the arcsecond scale ionized disk. This may be the point at which the filament W1 feeds the disk.

In this study, the presence of a wide angle (half-opening angle of ∼45°) outflow along the same (3 dimensional) axis as the jet is posited. The diffuse and blue filamentary structures on scales of $1.5''$–$4''$ to the N participate in this conical radial outflow (and are thus in front of the nucleus). Equivalently, the redshifted gas at the same distance to the SW is behind the nucleus and part of the redshifted conical outflow. Apart from this velocity structure, the conical outflow model is supported by the velocity gradients seen in the blueshifted (N) and redshifted (S) ionized gas seen in the regions $1''$–$4''$ from the nucleus. With a radial velocity of ∼400 km s^{-1}, the outflow requires to be powered by the AGN, but since the blue and red shifted cones are only partially filled with ionized gas, the ionized gas

would have to be entrained from the patchy and filamentary interstellar medium by a wide angle wind launched near the black hole. Each cone requires to be at least $3''$ in extent, and thus the crossing time is 0.6 Myr, significantly shorter than the lifetime of the M87 larger scale jet and lobes (Owen et al., 2000).

Many of the filaments seen in the inner $4''$ appear to cross the nucleus, corresponding to one of the following three cases: (a) those which follow the potential of the black hole, and thus likely truly enter the inner 5 pc; (b) those which enter the nucleus, but only in projection, as their bulk blueshifts are not changed as (projected) nuclear separation decreases; and (c) at least one mixed case where highly blueshifted filament participates in a systemic-velocity-offset quasi-Keplerian rotation as it crosses the nucleus in projection; for illustration, this is modeled as Keplerian rotation in a plane with inclination of $60°$. Two potential explanations are a gas filament with a large bulk velocity which approaches the nucleus at high inclination, or Keplerian rotating gas near the nucleus which is swept into the biconical outflow.

With respect to the inner ionized gas disk: if the M87 jet is intrinsically two-sided, then the (brighter due to Doppler boosting) NW jet is oriented toward us. For the inner ($<0.1''$) accretion disk to be perpendicular to the jet axis, it is expected that the SE half of the disk is the near side, and the NW the far side. If this is maintained, i.e. if the disk warp is 'slight', the same must be for the arcsecond scale ionized gas disk. Indeed, dust lanes seen in the HST images of Ford et al. (1994) led them to suggest that the SE side is the near side.

The twisted isophotes seen in the inner arcseconds of the ionized gas disk potentially resolve another long standing problem: the mismatch between the axes of the inner ionized gas disk and the prominent jet. This issue is extensively discussed in Jeter et al. (2019). The velocity maps in Fig. 4.2.4 provide clear evidence for twisted velocity isophotes in the inner arcsecond of the disk. The twist is clearest from PA $\sim42°$ at $0.''3$–$0.''5$ to PA $\sim90°$ at $0.''1$–$0.''2$. Inside this radius, there is a suggestion of a further twist: the value of this innermost PA is most clearly constrained using the residual maps of the best fit model (right panel of Fig. 5.4.2). Here, the residual over-subtraction is at PA $\sim17°$, perpendicular to the jet axis. Since the innermost resolved region is about ~5 pc, there is of course room for further twists down to the jet launching region around the black hole. For radii $\geq0.''3$, the redshifted side of the disk shows some indications for further twists in

the velocity isophotes, though at 10s of arcsecond scales there is a support for a PA close to 40° and inclination equal to the inner arcsecond disk.

The kinematic analysis clearly shows the presence of multiple velocity components (disk, outflow, and filaments) overlapping in the nucleus. Given this, it is dangerous to constrain the inclination of the disk using isophotal fits. The $H\alpha$ + [N II] and [O I] moment 0 maps do not show a clear and consistent inclined disk shape. In these, while the different intensity levels are highly non axi-symmetric, one gets more of an impression of a face-on, rather than inclined, disk. At least a part of this face-on appearance could be due to filament 8 passing through the nucleus in projection. Its 'zero' velocity gas would extend the intensity contours of the disk along its minor axis. To the N ionized gas in the outflow is seen even in the inner arcseconds, elongating the N-S extent at some radii. Morphologically, the disk is best constrained via its spiral arm structure, which can be seen both in intensity and kinematics. These spiral arms are better encompassed by a i = 25°, rather than i = 42° disk. The kinematics of the [O I] line in the inner $0\rlap{.}''2$ to $0\rlap{.}''6$ is slightly better fit with an inclination of $\sim$25° as compared to 42°. Finally, the kinematics of the large scale filaments W1 and W2, which extend from a few to tens of arcseconds from the nucleus, can be reasonably explained in most parts by a rotating disk with i = 25° (but not as well or consistently with a i = 42° disk). Together, the three results favor a relatively face-on disk rather than one at i $\sim$42°. This lower inclination disk is also consistent with the posited 3-dimensional direction of the jet. Though, given the warp in the PA of the disk, it is impossible to rule out a change in inclination inside the central resolution elements.

A precise measurement (with well defined errors) of the black hole mass via ionized gas kinematics is not possible due to the many morphological and kinematic complexities in the ionized gas, which have been discussed extensively in this work. Even removing the effects of the ionized filaments which cross the nucleus (sometimes only in projection), and the outflow component, the irregular shape of the disk, the non axis-symmetric velocities displayed by the disk, the twisted inner velocity isophotes, and the finding that the spiral arms are slightly redshifted from the diffuse gas in the inner disk, all preclude a sufficiently accurate determination of the inclination of the subarcsecond scale disk, and thus black hole mass.

Nevertheless, the deep and integral spectroscopy from MUSE allows to clarify and constrain previous contradictory black hole mass measurements: e.g., the high

mass black holes of G11, the EHT Collaboration, and Liepold et al. (2023) versus the low mass black hole of W13. First and foremost, it have been shown that the complexities of the nuclear ionized gas highly complicate the determination of an accurate measurement of the black hole mass from ionized gas kinematics, which immediately lends more weight to the high mass value. However, some indications can be leveraged from the new data, especially via the [O I] velocities. With the caveat of all the complexities involved, It seems to be no reason to favor a i = 42° disk over a lower (i ∼25°) one. However, several factors support, even if sometimes weakly, a disk inclination closer to 25°: (a) fits to the sub-arcsecond ionized gas disk with the *Kinemetry* package support inclinations closer to 20°–25°, a PA of ∼45°, with the disk velocities dominated by rotation; (b) a minimization of the differences between the observed velocity fields of the sub-arcsecond ionized gas disk and simulated velocity fields derived via *KinMSpy* over a range of black hole masses and inclinations, lends weak support to the scenario of a high mass black hole in a low inclination disk, as opposed to a low mass black hole in a higher (42°) inclination disk; (c) visual comparisons of the LBH i42 model and the HBH i25 model with the observed velocity fields and pv diagrams, also weakly support the HBH i25 model, though their predictions are very similar within the complexities, and large linewidths, of the emission lines; (d) morphologically, the spiral arms in the inner arcseconds of the ionized disk, which are the most plausible parts of the 'disk' involved in circular rotation, are better encompassed by a i = 25°, rather than i = 42° disk; (e) the outer ionized gas filaments on 10s of arcsecond scales can be relatively well fit with a rotating disk with i = 25°, but not with i = 42°. At these large nuclear distances, the rotation is dominated by the galaxy potential, so that there is no longer a degeneracy between black hole mass and inclination in the rotational fits. Finally, and independently, it can be noted that the lower inclination disk provides a more consistent alignment between the axes of the ionized gas disk, the well known jet, and the biconical outflow found here. Thus the most consistent explanation for the observed inner ionized gas rotating disk is a black hole with mass closer to 6.0×10^9 $M_\odot$ surrounded by a low (i ∼25°) inclination disk.

To reduce the tension between the G11 and W13 mass measurements, Jeter et al. (2019) have suggested intrinsic sub-Keplerian disk rotation of the ionized gas as a potential solution. The specific RIAF model proposed by these authors (over a

range of black hole masses and disk inclinations) was tested against the observed velocity field of the sub-arcsecond nuclear disk, and found the following: (a) the sub-Keplerian rotational velocities of RIAF models indeed allow a higher black hole mass in a given disk inclination as compared to Keplerian rotation models, but the specific value of Ω in the Jeter RIAF model is not sufficiently small to allow a HBH in a i $=42°$ RIAF disk to masquerade as a LBH in a i $=42°$ Keplerian disk; (b) the residual (observed minus model) velocity fields of Keplerian models were compared to those with RIAF models. Except for one masking scheme used (Gauss-fit masking), Keplerian models result in significantly smaller velocity residuals as compared to RIAF models when both black hole mass and inclination can freely vary. Reducing the value of Ω can solve the issues in item (a) above, but not item (b). Further, the disk outflow in the RIAF model should result in significant non-circular motions in the disk. However the *Kinemetry* fits to the sub-arcsecond ionized gas disk implies that the bulk of the velocities can be fit with pure rotation, i.e. non-rotative contributions are small. Thus overall, a HBH in a low inclination disk is a simpler and better-fit alternative to a HBH in a RIAF inflow.

Putting all the results together gives us a simple and consistent picture of the nucleus of M87. A black hole mass closer to $\sim$6.0–6.5 (rather than 3.5) billion solar masses (for a distance of 16.8 Mpc), together with a warped (at PA at least) sub-arcsecond ionized disk with inclination $\sim$25°. The PA of the innermost accretion disk seen in the residual [O I] velocity map suggests a disk axis aligned with the axes of both the jet and the (partially filled) nuclear radial biconical outflow. The disk inclination to the LOS matches that expected from Doppler boosting of the approaching jet. The kinematics of the ionized filaments at $4''$–$20''$ are reasonably well explained by a (partially filled) rotating disk with inclination 25°, though the several kinks and bubbles along their length point to the presence of other flow velocities and instabilities.

Chapter 7

Conclusion

The ionized gas kinematics close to the M87 nucleus is a complex mixture of different components: several filaments, many crossing the galaxy nucleus in projection; a partially filled biconical outflow; and a rotating disk affected by the black hole and the galaxy potential.

The ionized gas filaments can be traced on both large and small scales. Two large and prominent filaments, and several blobs with their own radial velocities, can be seen at large-scale. Closer to the nucleus, there are several shorter filaments; only one of them seems to participate in the rotation movement around the black hole, but it is located along the minor axis, and cannot be used to estimate the black hole mass.

The outflow can be approximated as a partially filled bicone; the approaching cone is located to the NE, and has a radial velocity of 400 km s^{-1} blueshifted respect to the systemic velocity; the receding cone is located to the SW, has a redshifted velocity of 400 km s^{-1}, and is less filled than the blueshifted cone. The outflow is also aligned with the galaxy jet.

The rotating disk has a position angle of 45° and an inclination in the range 20°–25°. Several spiral arms can be seen in both the intensity and the residual velocity maps. There is also a velocity isophote twist toward the nucleus that tends to be aligned with the galaxy jet.

The complex kinematics in M87 prevents to accurately measure the black hole mass of the galaxy using ionized gas emission lines as tracers. On the other hand,

there is no such a big difference between the velocity predictions from a disk rotating around a black hole mass of 6.0 $\times 10^9$ M$_\odot$ and inclination of 25°, and a 3.5 $\times 10^9$ M$_\odot$ and 42° disk.

Two main results are in favor of a 25° disk: the inclination range of 20°–25° that results from the program *Kinemetry*; and the statistics from the velocity residual maps, with varying black hole masses and inclinations, and whose minima tends to have inclinations close to 25°, specially at large scale; considering the foregoing, there is no reason to favor a model of a 3.5 $\times 10^9$ M$_\odot$ and 42° disk.

The results of this study helps to reconcile the contradictory results between the stellar and the ionized gas previous black hole mass measurements, giving more support to the stellar result. It also could give more insights for the discrepancy in the measurement of the black hole masses of similar galaxies. In a future work, an improvement of the measurement of the black hole mass in M87 using the stellar kinematics and a robust model such as the Schwarzschild method, could be made using both the WFM and the new NFM data sets.

Bibliography

Bacon, R., Accardo, M., Adjali, L., Anwand, H., Bauer, S., Biswas, I., Blaizot, J., Boudon, D., Brau-Nogue, S., Brinchmann, J., Caillier, P., Capoani, L., Carollo, C. M., Contini, T., Couderc, P., Daguisé, E., Deiries, S., Delabre, B., Dreizler, S., Dubois, J., Dupieux, M., Dupuy, C., Emsellem, E., Fechner, T., Fleischmann, A., François, M., Gallou, G., Gharsa, T., Glindemann, A., Gojak, D., Guiderdoni, B., Hansali, G., Hahn, T., Jarno, A., Kelz, A., Koehler, C., Kosmalski, J., Laurent, F., Le Floch, M., Lilly, S. J., Lizon, J. L., Loupias, M., Manescau, A., Monstein, C., Nicklas, H., Olaya, J. C., Pares, L., Pasquini, L., Pécontal-Rousset, A., Pelló, R., Petit, C., Popow, E., Reiss, R., Remillieux, A., Renault, E., Roth, M., Rupprecht, G., Serre, D., Schaye, J., Soucail, G., Steinmetz, M., Streicher, O., Stuik, R., Valentin, H., Vernet, J., Weilbacher, P., Wisotzki, L., and Yerle, N. (2010). The MUSE second-generation VLT instrument. 7735:773508.

Barth, A. J., Darling, J., Baker, A. J., Boizelle, B. D., Buote, D. A., Ho, L. C., and Walsh, J. L. (2016). Toward Precision Black Hole Masses with ALMA: NGC 1332 as a Case Study in Molecular Disk Dynamics. , 823(1):51.

Barth, A. J., Sarzi, M., Rix, H.-W., Ho, L. C., Filippenko, A. V., and Sargent, W. L. W. (2001). Evidence for a Supermassive Black Hole in the S0 Galaxy NGC 3245. , 555(2):685–708.

Bentz, M. C., Walsh, J. L., Barth, A. J., Yoshii, Y., Woo, J.-H., Wang, X., Treu, T., Thornton, C. E., Street, R. A., Steele, T. N., Silverman, J. M., Serduke, F. J. D., Sakata, Y., Minezaki, T., Malkan, M. A., Li, W., Lee, N., Hiner, K. D., Hidas, M. G., Greene, J. E., Gates, E. L., Ganeshalingam, M., Filippenko, A. V., Canalizo, G., Bennert, V. N., and Baliber, N. (2010). The Lick AGN Monitoring Project: Reverberation Mapping of Optical Hydrogen and Helium Recombination Lines. , 716(2):993–1011.

Bertola, F., Bettoni, D., Danziger, J., Sadler, E., Sparke, L., and de Zeeuw, T. (1991). Testing the Gravitational Field in Elliptical Galaxies: NGC 5077. , 373:369.

Bittner, A., Falcón-Barroso, J., Nedelchev, B., Dorta, A., Gadotti, D. A., Sarzi, M., Molaeinezhad, A., Iodice, E., Rosado-Belza, D., de Lorenzo-Cáceres, A., Fragkoudi, F., Galán-de Anta, P. M., Husemann, B., Méndez-Abreu, J., Neumann, J., Pinna, F., Querejeta, M., Sánchez-Blázquez, P., and Seidel,

M. K. (2019). The GIST pipeline: A multi-purpose tool for the analysis and visualisation of (integral-field) spectroscopic data. , 628:A117.

Boselli, A., Fossati, M., Longobardi, A., Consolandi, G., Amram, P., Sun, M., Andreani, P., Boquien, M., Braine, J., Combes, F., Côté, P., Cuillandre, J. C., Duc, P. A., Emsellem, E., Ferrarese, L., Gavazzi, G., Gwyn, S., Hensler, G., Peng, E. W., Plana, H., Roediger, J., Sanchez-Janssen, R., Sarzi, M., Serra, P., and Trinchieri, G. (2019). A Virgo Environmental Survey Tracing Ionised Gas Emission (VESTIGE). V. Properties of the ionised gas filament of M 87. , 623:A52.

Cappellari, M. (2017). Improving the full spectrum fitting method: accurate convolution with Gauss-Hermite functions. , 466(1):798–811.

Cappellari, M. and Copin, Y. (2003). Adaptive spatial binning of integral-field spectroscopic data using Voronoi tessellations. , 342(2):345–354.

Cappellari, M. and Emsellem, E. (2004). Parametric Recovery of Line-of-Sight Velocity Distributions from Absorption-Line Spectra of Galaxies via Penalized Likelihood. , 116(816):138–147.

Carroll, B. W. and Ostlie, D. A. (2007). *An Introduction to Modern Astrophysics*. 2nd (international) edition.

Davis, T. A. (2014). A figure of merit for black hole mass measurements with molecular gas. , 443(1):911–918.

Davis, T. A., Alatalo, K., Bureau, M., Cappellari, M., Scott, N., Young, L. M., Blitz, L., Crocker, A., Bayet, E., Bois, M., Bournaud, F., Davies, R. L., de Zeeuw, P. T., Duc, P.-A., Emsellem, E., Khochfar, S., Krajnović, D., Kuntschner, H., Lablanche, P.-Y., McDermid, R. M., Morganti, R., Naab, T., Oosterloo, T., Sarzi, M., Serra, P., and Weijmans, A.-M. (2013). The ATLAS^{3D} Project - XIV. The extent and kinematics of the molecular gas in early-type galaxies. , 429(1):534–555.

Di Matteo, T., Springel, V., and Hernquist, L. (2005). Energy input from quasars regulates the growth and activity of black holes and their host galaxies. , 433(7026):604–607.

Emsellem, E., Cappellari, M., Peletier, R. F., McDermid, R. M., Bacon, R., Bureau, M., Copin, Y., Davies, R. L., Krajnović, D., Kuntschner, H., Miller, B. W., and de Zeeuw, P. T. (2004). The SAURON project - III. Integral-field absorption-line kinematics of 48 elliptical and lenticular galaxies. , 352(3):721–743.

Emsellem, E., Krajnovic, D., and Sarzi, M. (2014). A kinematically distinct core and minor-axis rotation: the MUSE perspective on M87. , 445:L79–L83.

Event Horizon Telescope Collaboration (2019). First M87 Event Horizon Telescope Results. VI. The Shadow and Mass of the Central Black Hole. , 875(1):L6.

Event Horizon Telescope Collaboration (2022). First Sagittarius A* Event

Horizon Telescope Results. IV. Variability, Morphology, and Black Hole Mass. , 930(2):L15.

Falcón-Barroso, J., Bacon, R., Bureau, M., Cappellari, M., Davies, R. L., de Zeeuw, P. T., Emsellem, E., Fathi, K., Krajnović, D., Kuntschner, H., McDermid, R. M., Peletier, R. F., and Sarzi, M. (2006). The SAURON project - VII. Integral-field absorption and emission-line kinematics of 24 spiral galaxy bulges. , 369(2):529–566.

Ferrarese, L. and Ford, H. (2005). Supermassive Black Holes in Galactic Nuclei: Past, Present and Future Research. , 116(3-4):523–624.

Ferrarese, L. and Merritt, D. (2000). A Fundamental Relation between Supermassive Black Holes and Their Host Galaxies. , 539(1):L9–L12.

Ford, H. C., Harms, R. J., Tsvetanov, Z. I., Hartig, G. F., Dressel, L. L., Kriss, G. A., Bohlin, R. C., Davidsen, A. F., Margon, B., and Kochhar, A. K. (1994). Narrowband HST Images of M87: Evidence for a Disk of Ionized Gas around a Massive Black Hole. , 435:L27.

Gao, F., Braatz, J. A., Reid, M. J., Condon, J. J., Greene, J. E., Henkel, C., Impellizzeri, C. M. V., Lo, K. Y., Kuo, C. Y., Pesce, D. W., Wagner, J., and Zhao, W. (2017). The Megamaser Cosmology Project. IX. Black Hole Masses for Three Maser Galaxies. , 834(1):52.

Gavazzi, G., Boselli, A., Vílchez, J. M., Iglesias-Paramo, J., and Bonfanti, C. (2000). The filament of ionized gas in the outskirt of M87. , 361:1–4.

Gebhardt, K., Adams, J., Richstone, D., Lauer, T., Gultekin, K., Murphy, J., Faber, S., and Tremaine, S. (2011). The Black Hole Mass in M87 from Gemini/AO Observations. 217:422.05.

Gebhardt, K. and Thomas, J. (2009). The Black Hole Mass, Stellar Mass-to-Light Ratio, and Dark Halo in M87. , 700(2):1690–1701.

Graham, A. W. (2008). Fundamental Planes and the Barless M_{BH}-σ Relation for Supermassive Black Holes. , 680(1):143–153.

Gralla, S. E., Lupsasca, A., and Marrone, D. P. (2020). The shape of the black hole photon ring: A precise test of strong-field general relativity. , 102(12):124004.

Gültekin, K., Richstone, D. O., Gebhardt, K., Lauer, T. R., Tremaine, S., Aller, M. C., Bender, R., Dressler, A., Faber, S. M., Filippenko, A. V., Green, R., Ho, L. C., Kormendy, J., Magorrian, J., Pinkney, J., and Siopis, C. (2009). The M-σ and M-L Relations in Galactic Bulges, and Determinations of Their Intrinsic Scatter. , 698(1):198–221.

Harms, R. J., Ford, H. C., Tsvetanov, Z. I., Hartig, G. F., Dressel, L. L., Kriss, G. A., Bohlin, R., Davidsen, A. F., Margon, B., and Kochhar, A. K. (1994). HST FOS Spectroscopy of M87: Evidence for a Disk of Ionized Gas around a Massive Black Hole. , 435:L35.

Hollas, J. M. (2004). *Modern spectroscopy.* J. Wiley, 4th ed edition.

Jeter, B., Broderick, A. E., and McNamara, B. R. (2019). Impact of Accretion Flow Dynamics on Gas-dynamical Black Hole Mass Estimates. , 882(2):82.

Johannsen, T. and Psaltis, D. (2010). Testing the No-hair Theorem with Observations in the Electromagnetic Spectrum. II. Black Hole Images. , 718(1):446–454.

Kormendy, J. and Gebhardt, K. (2001). Supermassive black holes in galactic nuclei. In Wheeler, J. C. and Martel, H., editors, *20th Texas Symposium on relativistic astrophysics*, volume 586 of *American Institute of Physics Conference Series*, pages 363–381.

Krajnović, D., Cappellari, M., de Zeeuw, P. T., and Copin, Y. (2006). Kinemetry: a generalization of photometry to the higher moments of the line-of-sight velocity distribution. , 366(3):787–802.

Liepold, E. R., Ma, C.-P., and Walsh, J. L. (2023). Keck integral-field spectroscopy of m87 reveals an intrinsically triaxial galaxy and a revised black hole mass.

Macchetto, F., Marconi, A., Axon, D. J., Capetti, A., Sparks, W., and Crane, P. (1997). The Supermassive Black Hole of M87 and the Kinematics of Its Associated Gaseous Disk. , 489(2):579–600.

Marconi, A. and Hunt, L. K. (2003). The Relation between Black Hole Mass, Bulge Mass, and Near-Infrared Luminosity. , 589(1):L21–L24.

Morison, I. (2008). *Introduction to Astronomy and Cosmology.* Manchester Physics Series. Wiley.

Murphy, J. D., Gebhardt, K., and Adams, J. J. (2011). Galaxy Kinematics with VIRUS-P: The Dark Matter Halo of M87. , 729(2):129.

Narayan, R. and Yi, I. (1995). Advection-dominated Accretion: Underfed Black Holes and Neutron Stars. , 452:710.

Owen, F. N., Eilek, J. A., and Kassim, N. E. (2000). M87 at 90 Centimeters: A Different Picture. , 543(2):611–619.

Pagotto, I., Corsini, E. M., Sarzi, M., Pagani, B., Dalla Bontà, E., Morelli, L., and Pizzella, A. (2019). A catalogue of nuclear stellar velocity dispersions of nearby galaxies from Hα STIS spectra to constrain supermassive black hole masses. , 483(1):57–69.

Rusli, S. P., Thomas, J., Erwin, P., Saglia, R. P., Nowak, N., and Bender, R. (2011). The central black hole mass of the high-σ but low-bulge-luminosity lenticular galaxy NGC 1332. , 410(2):1223–1236.

Saglia, R. P., Opitsch, M., Erwin, P., Thomas, J., Beifiori, A., Fabricius, M., Mazzalay, X., Nowak, N., Rusli, S. P., and Bender, R. (2016). The SINFONI

Black Hole Survey: The Black Hole Fundamental Plane Revisited and the Paths of (Co)evolution of Supermassive Black Holes and Bulges. , 818(1):47.

Sargent, W. L. W., Young, P. J., Boksenberg, A., Shortridge, K., Lynds, C. R., and Hartwick, F. D. A. (1978). Dynamical evidence for a central mass concentration in the galaxy M87. , 221:731–744.

Sarzi, M., Falcón-Barroso, J., Davies, R. L., Bacon, R., Bureau, M., Cappellari, M., de Zeeuw, P. T., Emsellem, E., Fathi, K., Krajnović, D., Kuntschner, H., McDermid, R. M., and Peletier, R. F. (2006). The SAURON project - V. Integral-field emission-line kinematics of 48 elliptical and lenticular galaxies. , 366(4):1151–1200.

Sarzi, M., Spiniello, C., La Barbera, F., Krajnović, D., and van den Bosch, R. (2018). MUSE observations of M87: radial gradients for the stellar initial-mass function and the abundance of sodium. , 478(3):4084–4100.

Schnorr-Müller, A., Storchi-Bergmann, T., Nagar, N. M., Robinson, A., and Lena, D. (2017). Gas inflows towards the nucleus of NGC 1358. , 471(4):3888–3898.

Schnorr Müller, A., Storchi-Bergmann, T., Riffel, R. A., Ferrari, F., Steiner, J. E., Axon, D. J., and Robinson, A. (2011). Gas streaming motions towards the nucleus of M81. , 413(1):149–161.

Smith, M. D., Bureau, M., Davis, T. A., Cappellari, M., Liu, L., North, E. V., Onishi, K., Iguchi, S., and Sarzi, M. (2019). WISDOM project - IV. A molecular gas dynamical measurement of the supermassive black hole mass in NGC 524. , 485(3):4359–4374.

Smith, M. D., Bureau, M., Davis, T. A., Cappellari, M., Liu, L., Onishi, K., Iguchi, S., North, E. V., Sarzi, M., and Williams, T. G. (2021). WISDOM project - VII. Molecular gas measurement of the supermassive black hole mass in the elliptical galaxy NGC 7052. , 503(4):5984–5996.

Thater, S., Krajnović, D., Nguyen, D. D., Iguchi, S., and Weilbacher, P. M. (2020). Testing the robustness of black hole mass measurements with ALMA and MUSE. 353:199–202.

van den Bosch, R. C. E., van de Ven, G., Verolme, E. K., Cappellari, M., and de Zeeuw, P. T. (2008). Triaxial orbit based galaxy models with an application to the (apparent) decoupled core galaxy NGC 4365. , 385(2):647–666.

Vasiliev, E. and Valluri, M. (2020). A New Implementation of the Schwarzschild Method for Constructing Observationally Driven Dynamical Models of Galaxies of All Morphological Types. , 889(1):39.

Vazdekis, A., Sánchez-Blázquez, P., Falcón-Barroso, J., Cenarro, A. J., Beasley, M. A., Cardiel, N., Gorgas, J., and Peletier, R. F. (2010). Evolutionary stellar population synthesis with MILES - I. The base models and a new line index system. , 404(4):1639–1671.

Vestergaard, M. (2004). Black-Hole Mass Measurements. 311:69.

Walker, R. C., Hardee, P. E., Davies, F. B., Ly, C., and Junor, W. (2018). The Structure and Dynamics of the Subparsec Jet in M87 Based on 50 VLBA Observations over 17 Years at 43 GHz. , 855(2):128.

Walsh, J. L., Barth, A. J., Ho, L. C., and Sarzi, M. (2013). The M87 Black Hole Mass from Gas-dynamical Models of Space Telescope Imaging Spectrograph Observations. , 770(2):86.

Werner, N., Simionescu, A., Million, E. T., Allen, S. W., Nulsen, P. E. J., von der Linden, A., Hansen, S. M., Böhringer, H., Churazov, E., Fabian, A. C., Forman, W. R., Jones, C., Sanders, J. S., and Taylor, G. B. (2010). Feedback under the microscope-II. Heating, gas uplift and mixing in the nearest cluster core. , 407(4):2063–2074.

Young, P. J., Westphal, J. A., Kristian, J., Wilson, C. P., and Landauer, F. P. (1978). Evidence for a supermassive object in the nucleus of the galaxy M87 from SIT and CCD area photometry. , 221:721–730.

Zhao, J.-H., Morris, M. R., Goss, W. M., and An, T. (2009). Dynamics of Ionized Gas at the Galactic Center: Very Large Array Observations of the Three-dimensional Velocity Field and Location of the Ionized Streams in Sagittarius A West. , 699(1):186–214.

Appendix A

# Comparison between the data from STIS and MUSE

Previous ionized gas based measurements of the black hole mass in M87 used aperture (Harms et al., 1994) or slit spectra (Macchetto et al., 1997; Walsh et al., 2013) from instruments on HST. In this work, MUSE data cubes were used; these new data have several advantages. MUSE is a relatively high throughput instrument on a 8 meter class telescope: in collecting area the VLT is about 11 times larger than HST. In AO mode, MUSE delivers a higher spatial resolution than STIS.

The STIS data used in Walsh et al. (2013) consists of spectra in five parallel slits, one of them crossing the nucleus of the galaxy, whereas the MUSE NFM data cube fully samples the inner $8'' \times 8''$. The larger FOV and full spatial sampling allows a more comprehensive analysis along any PA. Furthermore, the MUSE data covers a larger wavelength range.

The only drawback of the data set is that MUSE has a slightly lower spectral resolution as compared to previous HST instruments used for such studies.

However, in a massive elliptical like M87, with relatively large velocities and velocity dispersions, the MUSE spectral resolution is sufficient to accurately resolve and measure gradients in these.

Figure A0.1 compares the pv diagrams obtained from the STIS data of Walsh et al. (2013) and our MUSE data along a nuclear slit at PA 51° (the slit PA
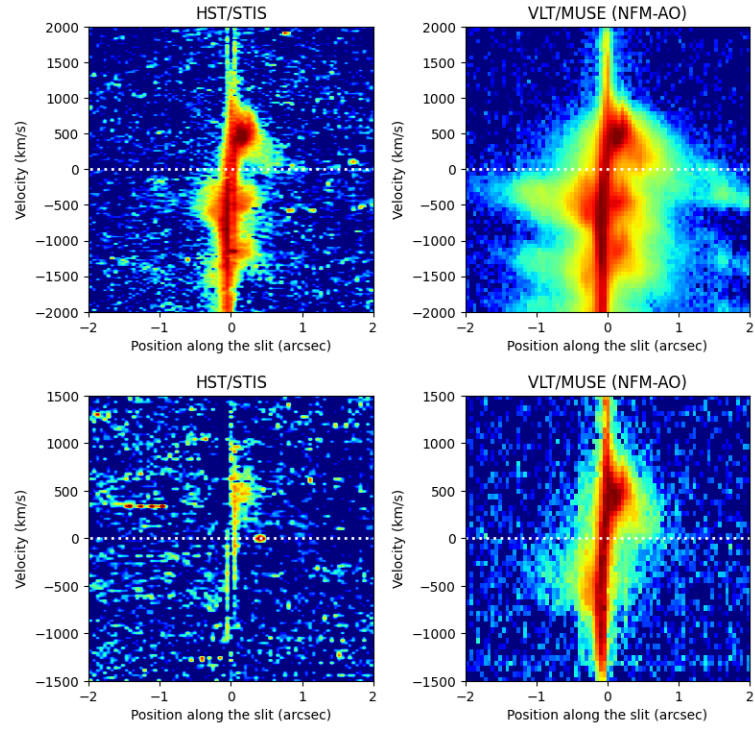
Figure A0.1: PV diagrams obtained from previous HST/STIS long-slit spectra and the VLT/MUSE-NFM-AO data cube used in this work.

used by W13). The upper and bottom panels are the spectra of, respectively, the [N II] $\lambda6583$ and [O I] $\lambda6300$ emission lines. Note the improvement of the quality of the data, especially in the weaker [O I] $\lambda6300$ line.